LIFETIME CONTROL IN SILICON THROUGH FOCUSED LASER BEAM DAMAGE

G. H. Schwuttke, Principal Investigator, 914-897-3140

International Business Machines Corporation
East Fishkill Laboratories
Hopewell Junction, New York 12533

Final Report
June 30, 1979

prepared by

G. H. Schwuttke and K. H. Yang

Modification No. P00005
to
Contract No. N00173-76-C-0303
Effective Date of Contract: May 1, 1978
Contract Expiration Date: June 30, 1979

Sponsored by

Defense Advanced Research Projects Agency (DARPA)
DARPA Order No. 3231, Program Code No. 8D10
Form Approved Budget Bureau No.: 22-R0293

UNCLASSIFIED

SECURITY CLASSIFICATION OF THIS PAGE (When Data Entered)

REPORT DOCUMENTATION PAGE	READ INSTRUCTIONS BEFORE COMPLETING FORM
1. REPORT NUMBER: Final rept. 1 May 78-30 apr 79	2. GOVT ACCESSION NO. / 3. RECIPIENT'S CATALOG NUMBER
4. TITLE (and Subtitle): LIFETIME CONTROL IN SILICON THROUGH FOCUSED LASER BEAM DAMAGE	5. TYPE OF REPORT & PERIOD COVERED: Final Report May 1, 1978-April 30, 1979
	6. PERFORMING ORG. REPORT NUMBER: TR#-22.2290
7. AUTHOR(s): G. H. Schwuttke and K. H. Yang	8. CONTRACT OR GRANT NUMBER(s): Modification #P00005 to Contract #N00173-76-0303
9. PERFORMING ORGANIZATION NAME AND ADDRESS: IBM CORPORATION, Data Systems Division, E. Fishkill Labs., Hopewell Junction, New York 12533	10. PROGRAM ELEMENT, PROJECT, TASK AREA & WORK UNIT NUMBERS: Program Element No.61101E, Program Code No. 8D10, DARPA Order No. 3231
11. CONTROLLING OFFICE NAME AND ADDRESS: Defense Advanced Research Projects Agency, Materials Sciences Office, 1400 Wilson Blvd., Arlington, Virginia 22209	12. REPORT DATE: 30 June 1979
	13. NUMBER OF PAGES: 91
14. MONITORING AGENCY NAME & ADDRESS (if different from Controlling Office): Naval Research Laboratory, Code 5261, P. R. Reid, Washington, D.C. 20375 (12) 92p.	15. SECURITY CLASS. (of this report): Unclassified
	15a. DECLASSIFICATION/DOWNGRADING SCHEDULE

16. DISTRIBUTION STATEMENT (of this Report)

Approved for public release, distribution unlimited

17. DISTRIBUTION STATEMENT (of the abstract entered in Block 20, if different from Report)

18. SUPPLEMENTARY NOTES

19. KEY WORDS (Continue on reverse side if necessary and identify by block number)

ion implantation
laser annealing
minority carrier lifetime
laser damage
gettering

20. ABSTRACT (Continue on reverse side if necessary and identify by block number)

Minority carrier lifetime and resistivity engineering in silicon through use of high power laser beams is described. Unique doping profiles are produced through 80 Kev $As^{(+)}$ implantations followed by laser annealing. Minority carrier lifetime distributions on silicon surfaces are substantially improved through laser damage gettering. Laser operating conditions to obtain optimum lifetime and resistivity engineering effects are given.

DD FORM 1 JAN 73 1473 EDITION OF 1 NOV 65 IS OBSOLETE

UNCLASSIFIED

SECURITY CLASSIFICATION OF THIS PAGE (When Data Entered)

401914

TABLE OF CONTENTS

CHAPTER II

LIST OF INVESTIGATORS

The project is supervised by Dr. G. H. Schwuttke, Principal Investigator. The following people contributed to the work in the report.

Dr. K. H. Yang	Chief Investigator
Mr. C. P. Schneider	Electrical Characterization
Mr. H. Steimel	Electron Microscopy Support
Mrs. S. Focht	Programming and Data Organization

HIGHLIGHTS

CHAPTER I

Laser annealing of 80 keV As^+ implanted layers is studied for different laser energies, laser spot sizes, and dopant concentrations.

Impurity distributions and dopant profiles are measured before and after laser annealing through 2MeV He^4 backscattering and spreading resistance techniques.

He^4 backscattering and spreading resistance measurements reveal that 100% of the arsenic dopant atoms are at substitutional lattice sites after laser annealing.

For an arsenic implantation of As^+ 10^{16} ions/cm^2, and a junction depth of 0.25 μm, 0.35 μm or 0.6 μm maximum achieved dopant concentrations are 8×10^{20} As/cm^3, 5×10^{20} As/cm^3 and 2×10^{20} As/cm^3. The corresponding sheet resistivities are 16.3, 15.8, 12.0 Ω/□.

For an arsenic implantation at 80 keV of As^+ 10^{15} ions/cm^2, a junction depth of 0.33 μm, 0.49 μm, or 0.75 μm, maximum arsenic concentrations of 7×10^{19}, 3×10^{19}, and 2×10^{19} are achieved. Corresponding sheet resistivities are 86.0, 73.2, 61.1 Ω/□.

Crystal perfection of annealed layers is investigated through transmission electron microscopy. Structure transitions from the implanted amorphous state to the polycrystalline or to the single crystal state are studied and requirements to achieve single crystal regrowth are determined.

Transition to single crystal is achieved for energies large enough to melt the implanted amorphous layer. Transition energies for laser annealing, where grown single crystal regions co-exist with grown polycrystalline areas, are determined. Interference effects which produce lateral non-uniformities in the annealed layer are studied.

For an implantation dose of As^{+} $10^{16}/cm^{2}$, implanted with an energy of 80 keV, laser annealed with a spot size of 180 μm, single crystal regrowth is obtained for an incident laser power of about 2.2 joules/cm^{2}.

The corresponding value for As^{15}/cm^{3} is 4.3 joules/cm^{2}.

Junction uniformity of laser-annealed junctions is analyzed. Local variations in junction depth are correlated with instabilities in the laser pulse which lead to non-uniform structural changes in the annealed layer and to local variations in junction depth.

It is also found that the implantation dose of the ion implanted layer influences its annealing behavior.

Annealed layers show better crystal perfection and better junction uniformity for larger laser spot sizes used for annealing.

CHAPTER II

Controlled laser damage -- produced on silicon wafer backsides -- before high temperature processing, is investigated as a means to improve minority carrier lifetime distribution on wafer frontsides.

The damage is produced with a Q-switch Nd-YAG laser operated at a wavelength of 1.06 μm. The damage is arranged in a pattern of parallel scan lines at constant spacing.

Optimum damage conditions for laser gettering are found for a damage depth of 5 to 10 μm and a scan line spacing of 0.5 to 1 mm. The corresponding energy density to produce this damage is 9 to 15 joules/cm^2.

For optimum damage conditions excellent gettering results are obtained.

The effectiveness of laser gettering is shown to depend on the amount of damage produced in the silicon.

Important damage parameters are identified as damage depth and scan line spacing.

For low laser power, sufficient to produce surface melting, the amount of damage in the wafer is small and gettering is not apparent.

For large laser power, sufficient to cause silicon evaporation (kerf cutting), substantial damage is produced and gettering becomes effective during subsequent high temperature processing.

The gettering arises from the strain fields and defects generated by the laser beam through local heating. During high-temperature processing large number of dislocations are produced by such damage sites and, accordingly, gettering becomes effective.

For too much damage (20 μm deep) dislocations thus generated slip to the wafer frontside and as a result lifetime degrades.

FOREWORD

This report describes the second and final part of the work done to Modification No. P00005 under Contract No N00173-76-C-0303, entitled "Lifetime Control in Silicon Through Focused Laser Beam Damage." The first part of the work under Modfication No. P00005 is summarized in Technical Report No. 1. The Highlights and the Table of Contents of Technical Report No. 1 are given in the Appendix.

This final report describes two applications of high power laser beams to semiconductor processing. The work relies on some unique properties of the material produced by laser heating followed by subsequent rapid cooling.

When a laser beam arrives over a localized silicon surface area the material below the beam rapidly increases in temperature. Two effects can happen, depending on the power input:

1) The power input is controlled such that the surface temperature first reaches the melting point of silicon and melting commences. Subsequently, the temperature in the melt rises above the melt temperature but stays below the boiling temperature. A superheated melt is formed. One interesting property of such a superheated

melt is its higher than normal solubility limit for silicon dopant atoms. Such dopants, pre-depositioned on the silicon surface by ion implantation or other techniques, dissolve in the melt. Upon cooling and crystal regrowth all dopant atoms are incorporated substitutionally into the silicon crystal. Using this effect, resistivity engineering in the silicon leads to unique doping profiles. This work is described in the first chapter of this report.

2) The power input is high, such that the material below the beam is evaporated and a kerf is cut. The depth of the kerf depends on the power input. Rapid cooling of the kerf upon moving the laser beam introduces localized strain and dislocations into the silicon. Subsequent high-temperature annealing, for instance, during semiconductor processing, generates large amounts of additional dislocations. This effect can be exploited to achieve minority carrier lifetime engineering in the silicon. This work is described in Chapter II of the final report.

An overview of the work performed and the results obtained are given in the section entitled "Highlights".

CHAPTER I

CHARACTERISTICS OF AS^+ IMPLANTED SILICON AFTER LASER ANNEALING

CHARACTERISTICS OF AS^+ IMPLANTED SILICON AFTER LASER ANNEALING

1.0 INTRODUCTION

Laser annealing of ion implanted silicon is an area of active research (1-8). The technique is useful in producing high concentration dopant profiles free of implantation damage. The perfection obtained in the implanted layer is the result of liquid phase epitaxial regrowth of a surface which is melted through the incident laser light (1,4,5,8).

In liquid phase epitaxy, as achieved with the help of pulsed laser radiation, a main concern is the spatial uniformity of crystalline perfection and also of the impurity distribution obtained in the annealed layer. This concern comes from the fact that the energy distribution of a focused laser beam operating in the TEM mode has a Gaussian distribution (5,8,9). Such a non-uniform energy distribution may cause non-uniformity of the crystalline layer perfection and of the impurity distribution in the annealed area. To minimize such problems, overlapping of successive pulses along a laser scan and overlapping between neighboring scans is used (1,5,6,8,9,10). In general, such overlapping can achieve a contiguous recrystallized layer of single crystal perfection.

While a great deal of effort has been expanded in obtaining high concentration dopant profiles through laser annealing, considerably less work has been done in studying the junction uniformity obtained through this technique. Junction uniformity is one of the important requirements for planar device fabrication. Therefore, this study investigates junction uniformity obtainable as a function of the laser power, of the spot size of the laser beam, and of the implantation dose. In addition, dopant distribution, surface morphology, and crystal perfection in the annealed layer are also investigated.

2.0 EXPERIMENTAL

Silicon wafers of <100> orientation, doped with boron to a resistivity of 2 Ω-cm, are used. These wafers are ion implanted at 80 keV with doses of 10^{15} and 10^{16} As /cm^2. The As implanted wafers are subsequently annealed with a Nd:YAG laser using a wavelength of 1.06 μm. Two spot sizes, 180 and 60 μm, are used. For the first experiment (I) a 75 mm objective lens, and for the second, experiment (II) a 27 mm objective lens is used. The laser operating parameters for these two experiments are listed in Table I. In experiment I, laser annealing is performed at different pulse rates. The energy density changes according to the change of the pulse rate. The pulse width at 8 kHz

TABLE I. Laser Operating Parameters for Annealing of As^+ Implanted Silicon

PARAMETERS	EXPERIMENT I	EXPERIMENT II
$\frac{1}{e}$ spot size, μm	180	60
Recrystallized spot size, μm	50 ~ 70	10 ~ 20
Pulse rate, KHz	8 ~ 20	8
Energy density, J/cm^2	2.2 ~ 4.9*	3.4 ~ 5.2**
Scan speed, cm/sec	25	7.5 or 10
Line spacing, μm	40	7.5 or 10
% overlap	~ 50	~ 50

* Energy density changes according to pulse rate.

** Energy density adjusted by the analyzer attached to to laser.

is about 140 nsec. An additional change of energy density is achieved by an analyzer attached to the laser.

The degree of overlapping for successive pulses along a laser scan can be calculated from: $\ell = s/rf$, where s is the scan speed, r is the annealed spot size, and f is the pulse rate. The degree of overlapping between two neighboring scans can be adjusted through proper line spacing. The degree of overlapping used in this study is about 50%. Because of a relatively large annealed spot size, experiment I requires a high scan speed and a wide line spacing.

Impurity profiles obtained through laser annealing are investigated through spreading resistance and He backscattering measurements. The junction uniformity is examined by the bevel-and-stain technique. The stain solution used consists of 49% HF and 60 mg $CuSO_4$ in 30 ml H_2O. The crystal perfection of laser annealed layers is investigated in a transmission electron microscope operated at 200 keV.

3.0 RESULTS

3.1 Impurity Distribution in Annealed Layers

The impurity distribution in laser annealed As^+ implanted layers is evaluated by 2 Mev He^4 backscattering and

spreading resistance measurements. The backscattering data obtained are discussed first.

3.1.1 He^4 Backscattering Measurements

Typical backscattering spectra are shown in Fig. 1 for a 10^{16} As^+/cm^2 implanted sample annealed with a 180 μm spot size at 3.4 joules/cm^2. The as-implanted aligned spectrum shows double peaks near the silicon surface, indicating partial annealing of implantation damage during ion implantation. After laser annealing, the <110> channeling yield near the surface drops to about 3% of random yield. This indicates an excellent crystalline perfection obtained in the laser-annealed, implanted layer. Figure 1 shows also the occurrence of redistribution of the implanted As after laser annealing. In the as-implanted state, As is confined to a narrow layer with a peak near the surface. After laser annealing, As penetrates deeper into the wafer bulk. By comparing random and channeling spectra, it is found that nearly 100% of the As atoms occupy substitutional sites in the silicon lattice. The characteristics of the samples shown in Fig. 1 are observed for samples laser annealed with an energy density ranging 2.2 to 4.9 joules/cm^2.

The impurity distribution is plotted as a function of pulsed energy density in Fig. 2. Figure 2 shows that in the as-implanted state, As has a peak concentration at a depth

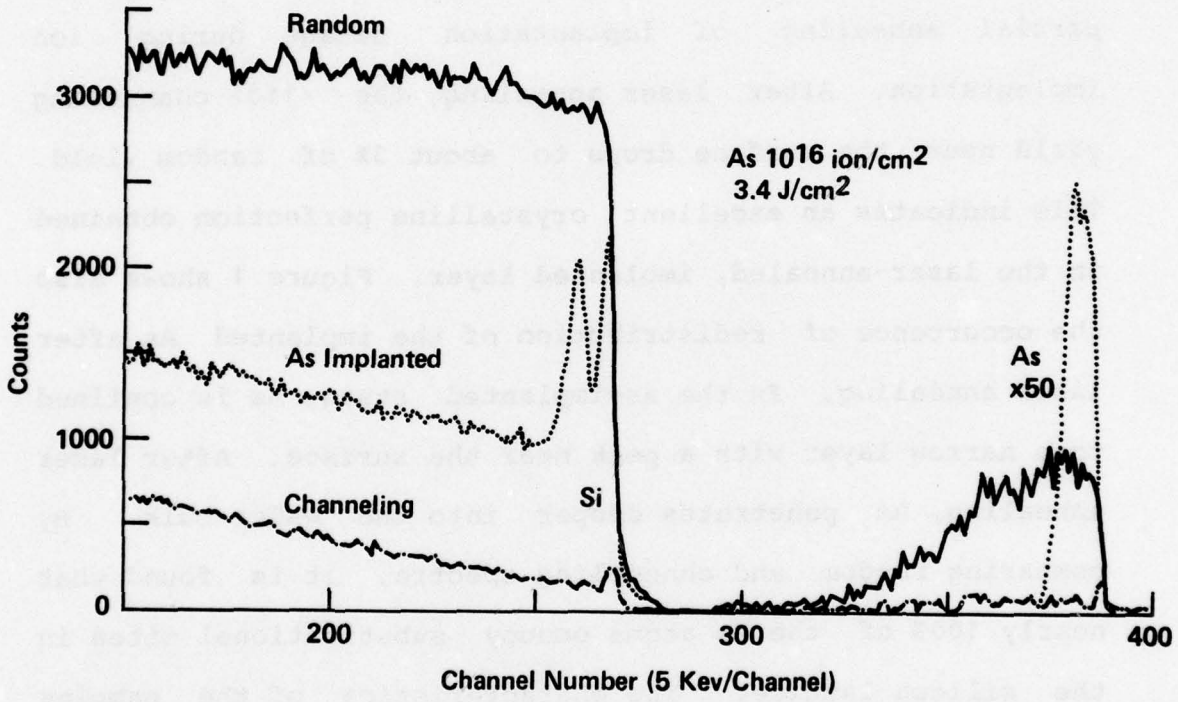

Fig. 1 He^4 backscattering spectra for a 10^{16} As/cm^2 implanted sample annealed with 180μm spot size at 3.4 joules/cm^2.

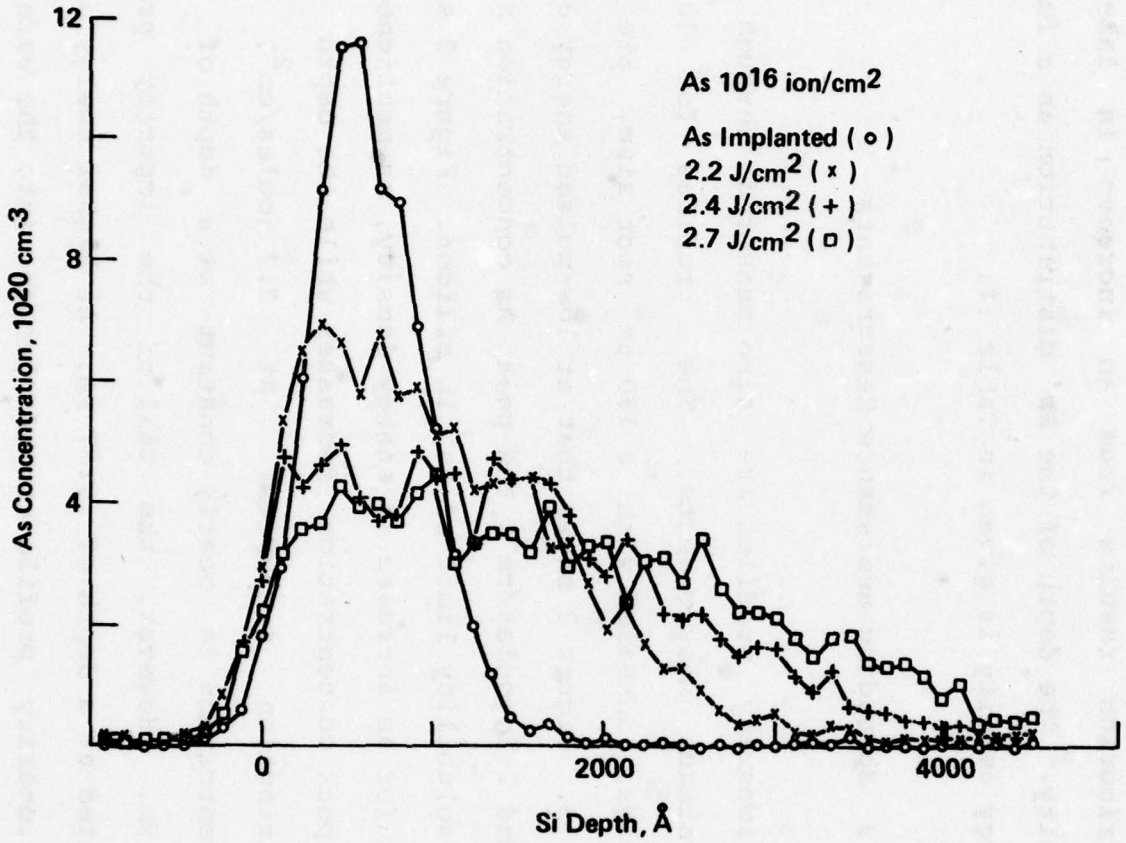

Fig. 2 Impurity distribution measured by He^4 backscattering for 10^{16} As/cm^2 implanted samples annealed with 180μm spot size at different energy densities.

around 500Å, corresponding to the mean projected range of 80 keV implanted As in silicon which is 481Å (12). During laser annealing, As atoms are driven into the wafer bulk and the peak concentration decreases. Such a decrease in peak concentration accompanied by an increase of As depth distribution results from an increase in laser energy density. The depth of the As distribution as a function of energy density is given in Table II.

3.1.2 Spreading Resistance Measurements

The impurity profiles are also measured through spreading resistance measurements. The profiles for 10^{16} As/cm^2 samples, annealed with a 180 μm spot size, are given in Fig. 3. Figure 3 shows that at low-pulsed energy densities, around 2.2 joules/cm^2, the peak As concentration approaches the solubility limit of As in silicon. Figure 3 shows also that for an increase in energy density, as mentioned before, the peak concentration decreases while the depth of the As distribution increases. At 3.2 joules/cm^2, the As concentration is nearly constant at a depth of less than 0.3 μm. However, the tail of the impurity profile is located at a depth of 0.57 μm. At higher energy densities, the impurity profile extends deeper into the wafer with a slight decrease in surface concentration. The characteristics of the impurity profiles obtained by spreading resistance measurements confirm the ones obtained

TABLE II Laser Annealing of As 10^{16} ions/cm^2 Implanted Silicon, Experiment I.

Sample	Pulse Rate KHz	Energy density, J/cm^2	Junction depth, μm			Active dose%	Sheet resist., Ω/□
			S.R.*	I.B.*	B.S.*		
A	8	4.9	0.97	1.00	0.96∿1.03	97	10.5
B	10	4.0	0.90	0.90	0.81∿0.88	96	10.8
C	12	3.4	0.80	0.80	0.66∿0.81	104	10.7
D	13	3.2	0.70	0.65	0.57∿0.78	94	11.8
E	14	3.0	0.59	0.60	0.50∿0.71	98	12.0
F	15	2.8	0.47	0.50	0.41∿0.55	99	12.9
G	16	2.7	0.44	0.42	0.38∿0.52	95	15.0
H	18	2.4	0.32	0.35	0.25∿0.33	93	15.8
I	20	2.2	0.27	0.25	0.20∿0.27	124	16.3

* S.R. refers to spreading resistance measurements

I.B. refers to ion backscattering measurements

B.S. refers to bevel-and stain measurements

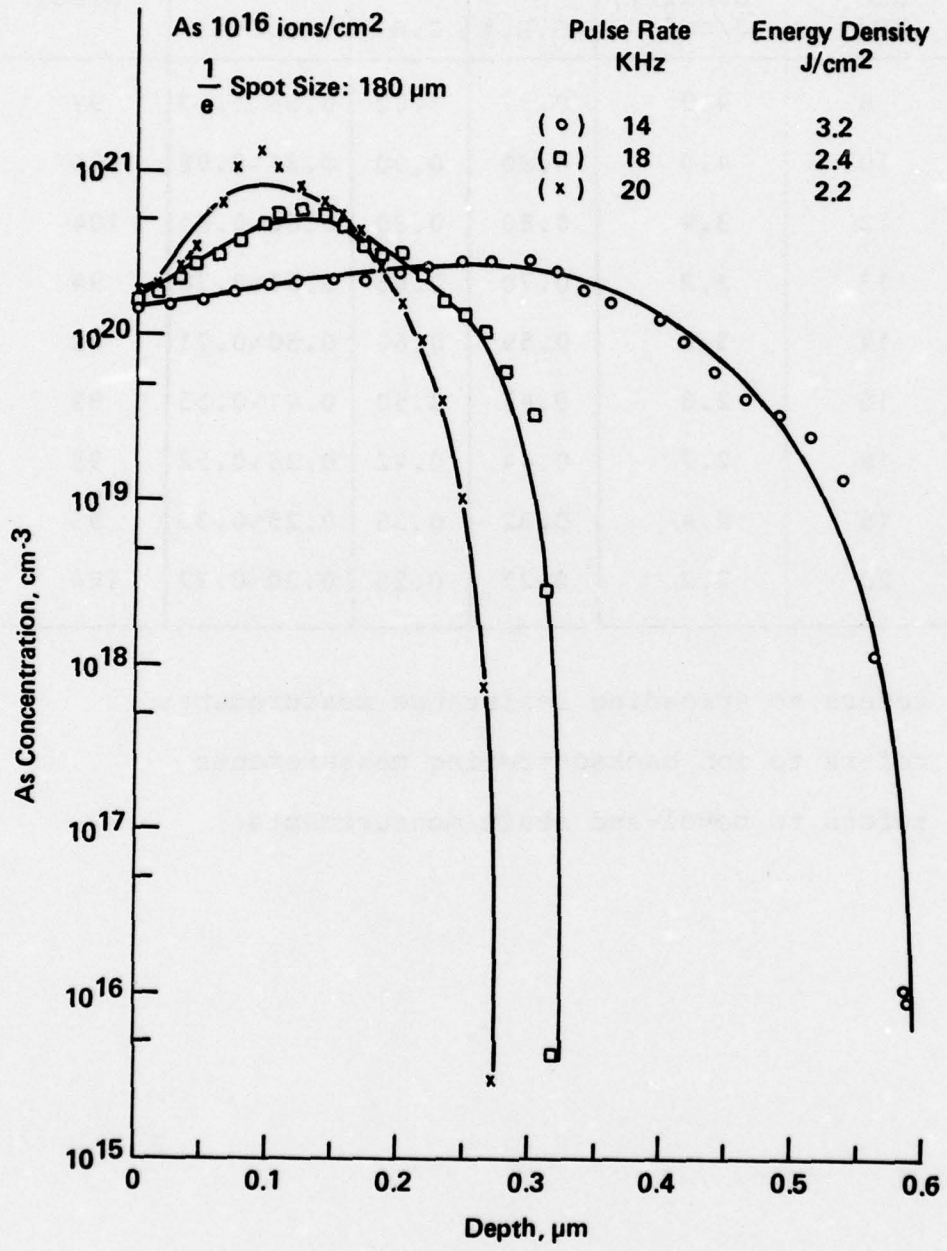

Fig. 3 Impurity profiles measured by spreading resistance measurements for 10^{16} As/cm^2 implanted samples annealed with 180μm spot size.

by He^4 backscattering, Fig. 2. The spreading resistance measurements indicate also that nearly 100% of the As atoms become electrically active after laser annealing. The depth of the impurity distribution, the active dose and the sheet resistance at different energy densities are summarized in Table II. It can be seen (Table II) that the depth of the impurity distribution, as measured through the spreading resistance technique, is in good agreement with the one obtained from He^4 backscattering measurements.

For 10^{15} As/cm^2 samples, annealed with a 180 μm spot size, the impurity profiles for different energy densities are shown in Fig. 4. The characteristics of the profiles in Fig. 4 are essentially the same as those shown in Fig. 3. However for the same energy density, the depth of As penetration is much shallower for the 10^{15} As/cm^2 samples. Below 3.4 joules/cm^2, laser annealing causes only partial activation of the electrically active atoms. The annealing threshold is therefore taken as 3.4 joules/cm^2 for the 10^{15} As/cm^2 samples. For the 10^{16} As/cm^2 samples this value is about 2.2 joules/cm^2. It appears that both the annealing threshold and the depth of impurity distribution are strongly dependent on implantation dose. Venkatesan, et al (6) explain that such a dose-dependent annealing behavior results from an increased absorption of the laser energy that occurs for higher As concentrations. The depth of the As distribution, the active dose, and the sheet

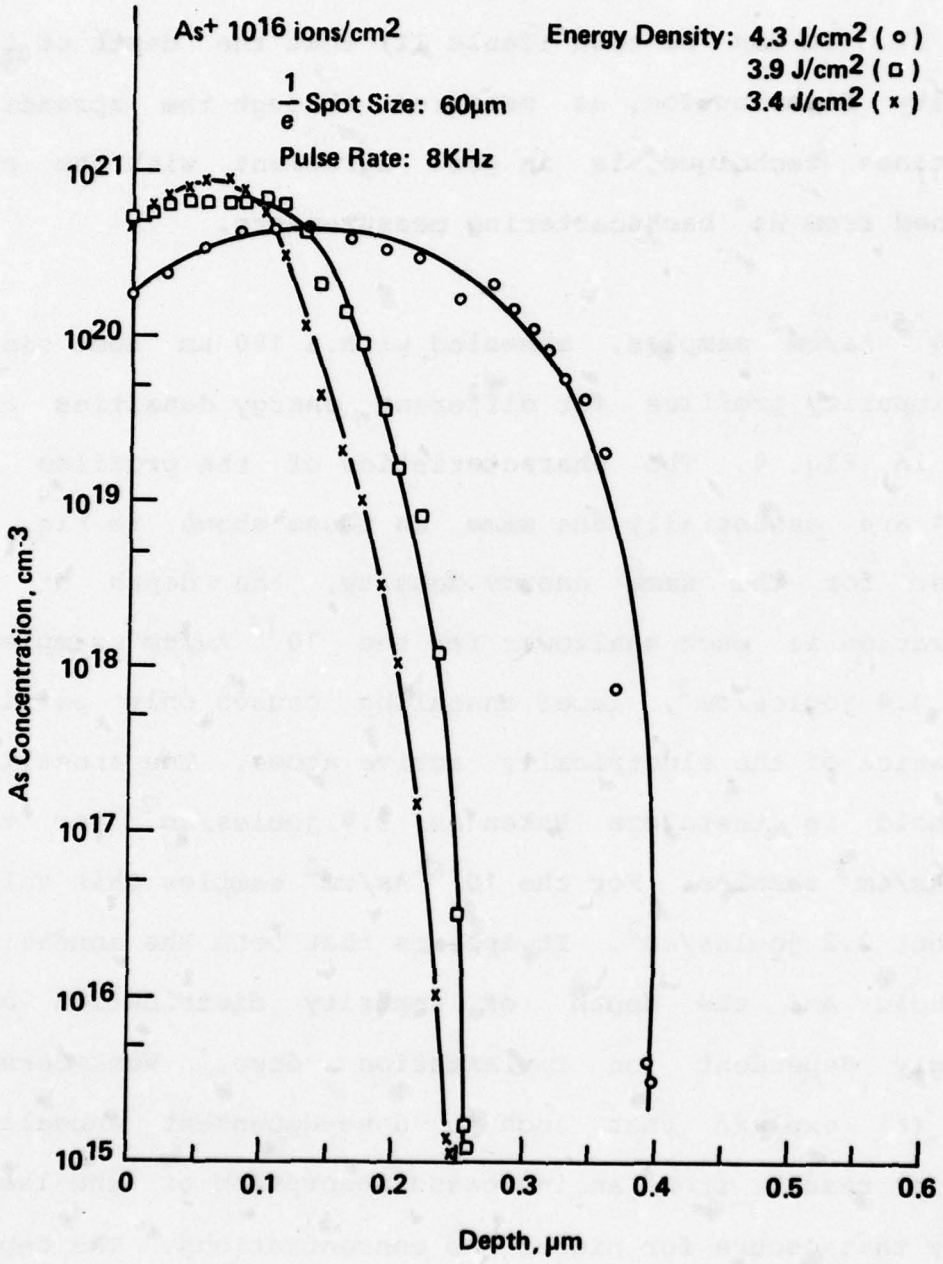

Fig. 4 Impurity profiles measured by spreading resistance measurements for 10^{15} As/cm^2 implanted samples annealed with 180μm spot size.

resistance as measured from spreading resistance measurements are summarized in Table III.

The behavior of laser annealing is also strongly influenced by the laser spot size. The impurity profiles for 10^{16} As^+/cm^2 implanted samples, annealed with a 60 μm spot size, are shown in Fig. 5. The depth of the impurity distribution, the active dose and the sheet resistance are summarized in Table IV. The annealing threshold is about 3.4 joules/cm^2. A comparison of Tables II and IV indicates that the annealing threshold increases and the depth of impurity penetration decreases as the spot size decreases.

For 10^{15} As/cm^2 implanted samples annealed with a 60 μm spot size, laser annealing with an energy density of up to 5.2 joules/cm^2 causes only partial activation of electrically active As atoms.

3.2 Surface Morphology and Crystal Perfection of Annealed Layers

The surface morphology and crystal perfection of laser annealed surfaces depends on several parameters, including the incident laser intensity, the spot size of the laser beam and also on the dopant concentration. A number of experiments were made to study the influence of these parameters on the annealing properties of implanted layers.

TABLE III. Laser Annealing As 10^{15} ions/cm^2

Implanted Silicon, Experiment I

Sample	Pulse Rate KHz	Energy Density, J/cm	Junction depth, μm S.R.*	B.S.*	Active dose, %	Sheet Resist Ω/□
A	8	4.9	0.75	0.64 ~ 0.90	119	61.05
B	10	4.0	0.49	0.48 ~ 0.64	103	73.21
C	12	3.4	0.33	0.33 ~ 0.38	98.0	86.04

*S.R. Refers to spreading resistance measurements

B.S. Refers to bevel-and-stain measurements

TABLE IV. Laser Annealing of As 10^{16} ions/cm^2

Implanted Silicon, Experiment II.

Sample	Pulse Rate, KHz	Energy density, J/cm	Junction depth, μm S.R.*	B.S.*	Active dose, %	Sheet resist Ω/□
A	8	4.3	0.39	0.39∿0.43	102	13.9
B	8	3.9	0.26	0.23∿0.28	101	19.4
C	8	3.4	0.24	0.22∿0.25	92	23.0

* S.R. refers to spreading resistance measurements

B.S. refers to bevel-and-stain measurements

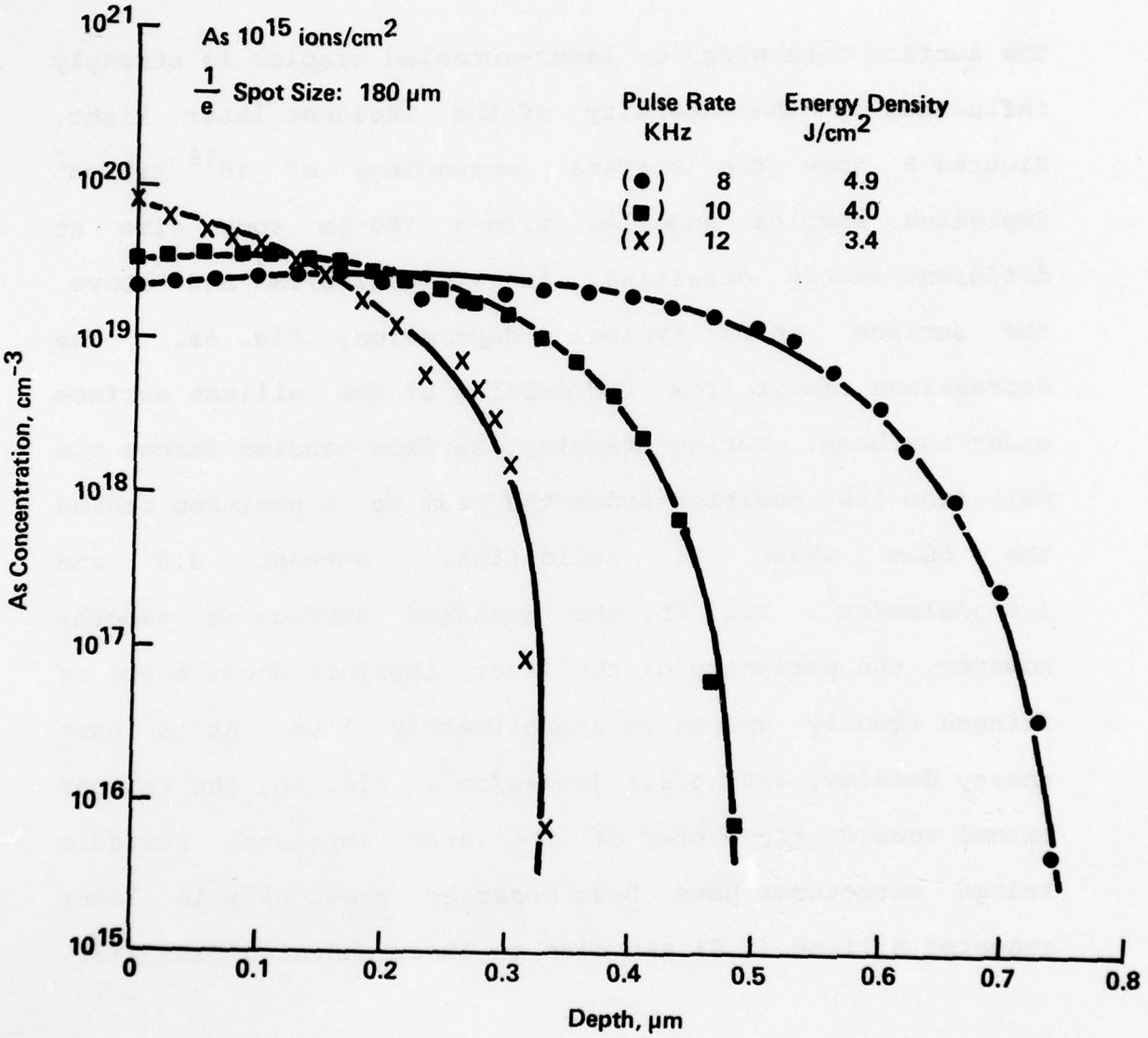

Fig. 5 Impurity profiles measured by spreading resistance measurements for 10^{16} As/cm^2 implanted samples annealed with 60μm spot size.

The dopant concentrations used are 10^{15} As^+/cm^2 and 10^{16} As^+/cm^2. Such surfaces were annealed with spot sizes of 180 μm and 60 μm.

3.3 Annealing of 10^{16} As^+/cm^2 Implanted Samples (180 μm Spot Size)

The surface morphology of laser-annealed samples is strongly influenced by the intensity of the incident laser light. Figures 6 show the surface morphology of 10^{16} As^+/cm^2 implanted samples annealed with a 180 μm spot size at different energy densities. At 4.0 joules/cm^2 and above, the surface shows typical depression, Fig. 6a. The depressions result from the melting of the silicon surface under the beam. During scanning, surface tension forces the melt from its position under the beam to a position behind the beam where it solidifies. Between 3.0 and 3.4 joules/cm^2, Fig. 6b, the annealed surface is smooth; however, the periphery of the laser imprints shows a set of fringes equally spaced at approximately 1 μm. At a lower energy density, around 2.2 joules/cm^2, Fig. 6c, the fringes extend toward the center of the laser imprints. Periodic fringe structures have been observed previously in laser annealed silicon (5,8) and also in laser-annealed GaAs (13).

The crystalline perfection of laser-annealed layers as shown in Figs. 6 were analyzed through electron microscopy. The

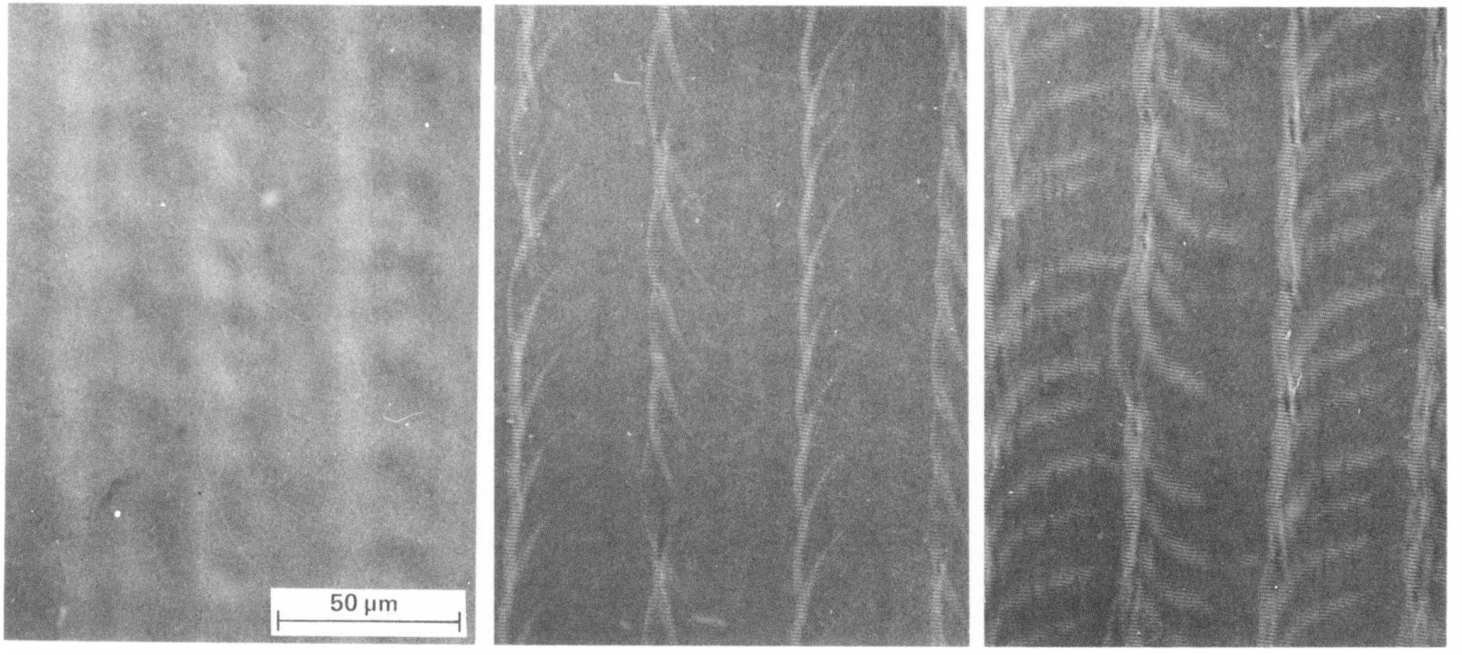

Fig. 6 Nomarski optical micrographs showing the surface morphology of 10^{16} As/cm^2 implanted samples annealed with 180µm spot size (a) 4.0, (b) 3.0, and (c) 2.2 joules/cm^2.

TEM analysis shows that samples annealed with an energy of 4.0 joules/cm^2 and above recrystallize into single crystal via epitaxial regrowth, Fig. 7a. No crystallographic defects are present in such layers. For the samples annealed between 3.0 and 3.4 joules/cm^2, a structure showing periodic fringes, as shown in Fig. 6b and 6c, is observed frequently. A TEM analysis of such fringes was made. These fringes appear as dark contrast in the electron micrograph indicating that they are surface ripples with a thickness larger than the surrounding area. Quite often, dislocations are observed to be associated with the fringed structure, Fig. 7b. As the energy density is lowered to 2.2 joules/cm^2, the fringe structure becomes more pronounced. TEM analysis shows that these structures represent areas where the crystallization is only partially complete. This is due to insufficient overlapping of the laser pulses, Fig. 7c. The TEM micrograph of Fig. 7c shows that both the completely crystallized and the partially crystallized areas alternate and form a pattern spaced with a distance of 1 μm. High magnification TEM micrographs show that the partially recrystallized areas contains dislocation loops of about 100 ~ 200Å in size, dislocations and polycrystalline material. However, between the fringes, the material is completely recrystallized and free of crystal defects, Fig. 7d. This observation is in good agreement with the one reported by Leamy, et al (5). These authors found also that laser annealing can be influenced by

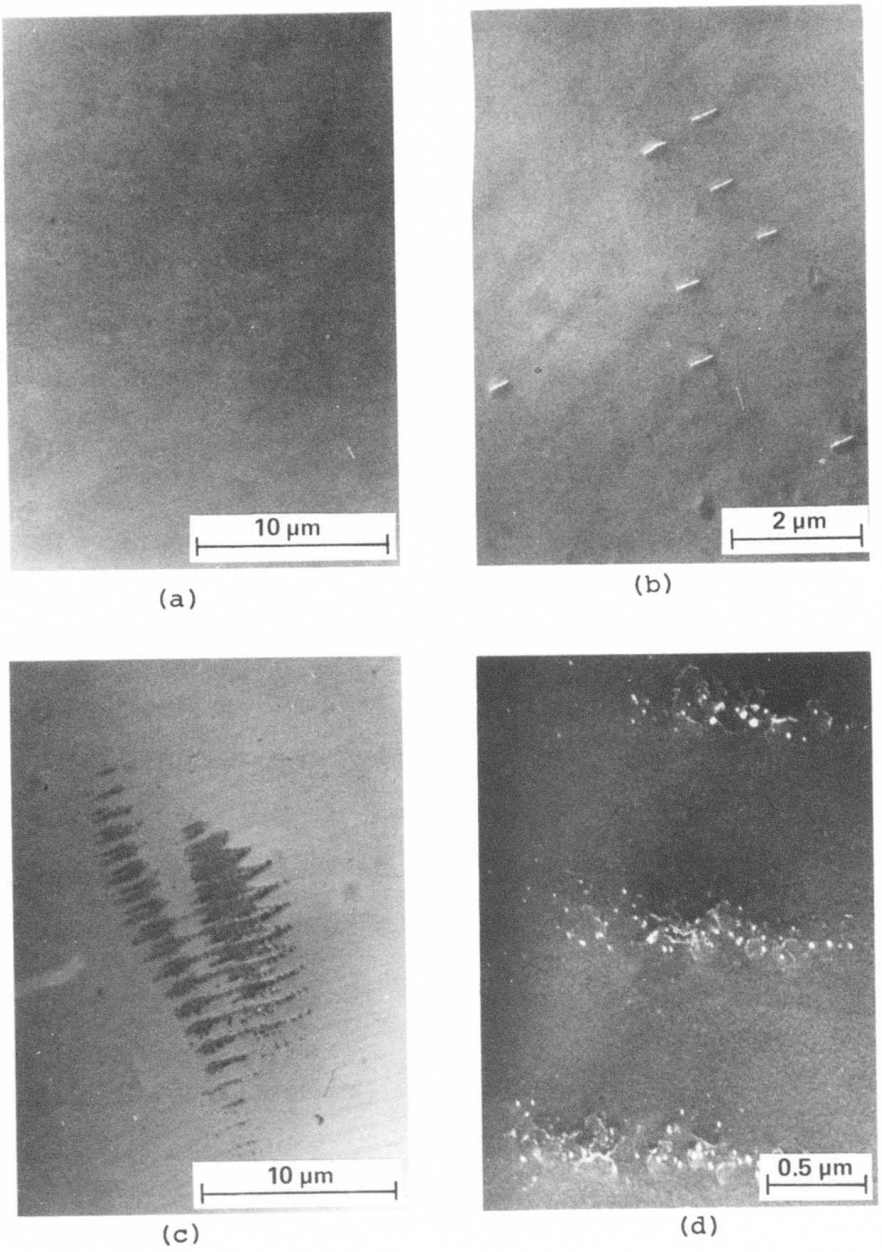

Fig. 7 TEM micrographs showing the crystal perfection of 10^{16} As/cm^2 samples annealed with 180μm spot size. (a) 4.0, (b) 3.0, (c) and (d) 2.2 joules/cm^2.

interference effects. The interference gives rise to intensity variations at the surface with a spacing corresponding to that of the wavelength of the laser radiation which is 1.06 μm. As the energy density decreases to 1.8 joules/cm^2, the annealed layer becomes polycrystalline. According to our measurements, the annealing threshold for the samples implanted with 10^{16} As^+/cm^2 is taken as 2.2 joules/cm^2. These data are summarized in Table V.

3.3.1 Annealing of 10^{15} As^+/cm^2 Implanted Samples (180 μm Spot Size)

The surface morphology of the 10^{15} As^+/cm^2 implanted sample is essentially the same as the one found for the 10^{16} As^+/cm^2 implanted samples shown in Fig. 6. However, a higher energy density is required for defect free annealing of 10^{15} As^+/cm^2 implanted samples if the same spot size is used.

Examples of 10^{15} As^+/cm^2 implanted samples annealed with a 180 μm spot size are shown in Figs. 8. Figure 8a shows that at 4.9 joules/cm^2, the annealed surface consists of depressions found at the location of the center of the laser pulses, and overlapping circular patterns at the periphery of the imprints of the pulses. Between 3.4 and 4.0 joules/cm^2, the surface is smooth and contains only

TABLE V. Laser Annealing: Spot Size 180μm
Implantation: 80 Kev, As^+ $10^{16}/cm^2$

Energy joules/cm^2	Surface Morphology	Large Perfection	Fig. No.
4	Smooth, circular pattern	Epi regrowth of total spot area, defect free	6a 7a
3 to 3.4	Smooth, fringes around periphery of annealed spot area	Fringes of surface ripples 500Å high; polysilicon alternates with single crystal area, spacing 1μm dislocations.	6b 7b
2.2*	Fringes extend toward center of spot	Polycrystalline and single crystal areas, dislocation loops	6c 7c, 7d
1.0	Fringes cover annealed area	Polysilicon in annealed area	-

*Annealing threshold at 2.2 joules/cm^2
Defect free epitaxial regrowth at 4.0 joules/cm^2

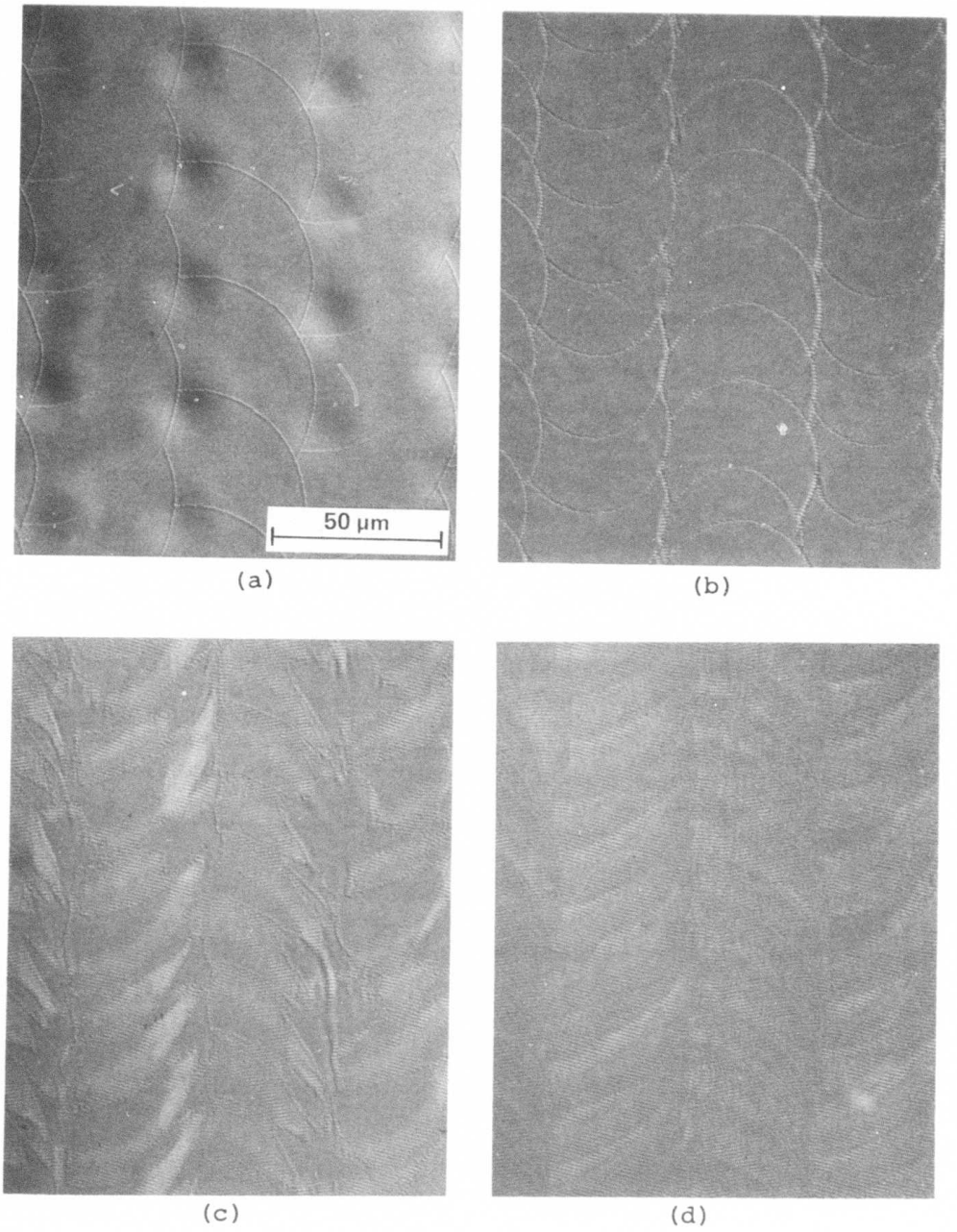

Fig. 8 Nomarski optical micrographs showing the surface morphology of 10^{15} As/cm^2 implanted samples annealed with 180µm spot size. (a) 4.9, (b) 3.4, (c) 3.0, and (d) 2.4 joules/cm^2.

overlapping circular patterns, Fig. 8b. At 3.0 joules/cm^2, a structure showing periodic fringes (spaced at 1 μm) starts to form at the periphery of the laser pulse imprints, Fig. 8c. At 2.4 joules/cm^2, the entire annealed surface is covered with the fringe structure, Fig. 8d.

The results of the TEM analysis of the samples shown in Figs. 8 are given in the micrographs of Figs. 9 to 10. It can be seen that defect-free epitaxial regrowth is achieved for the samples annealed with an energy of 4.9 joules/cm^2, Fig. 9a. At 3.4 joules/cm^2, annealing is still good but dislocations are frequently observed in the recrystallized layer, Fig. 9b. The annealing threshold for this case is taken as 3.4 joules/cm^2. As the energy density decreases to 3.0 joules/cm^2, the annealed layer consists mainly of the described fringe structure, Fig. 10a. The fringe structure lies predominantly at the periphery of the laser pulse imprints as shown in Fig. 8b. A portion of Fig. 10a, shown at higher magnification, is given in Fig. 10b. The spacing between two fringes, as measured from Fig. 10b, is 1.06 μm, equal to the wavelength of Nd:YAG radiation. Figure 10b shows also that the material between the fringes recrystallizes into single crystal. This indicates again that in this area the annealing threshold is exceeded during annealing, as discussed for the 10^{16} As^+/cm^2 implanted samples. The fringe structure contains polycrystalline silicon as evidenced by the electron diffraction pattern

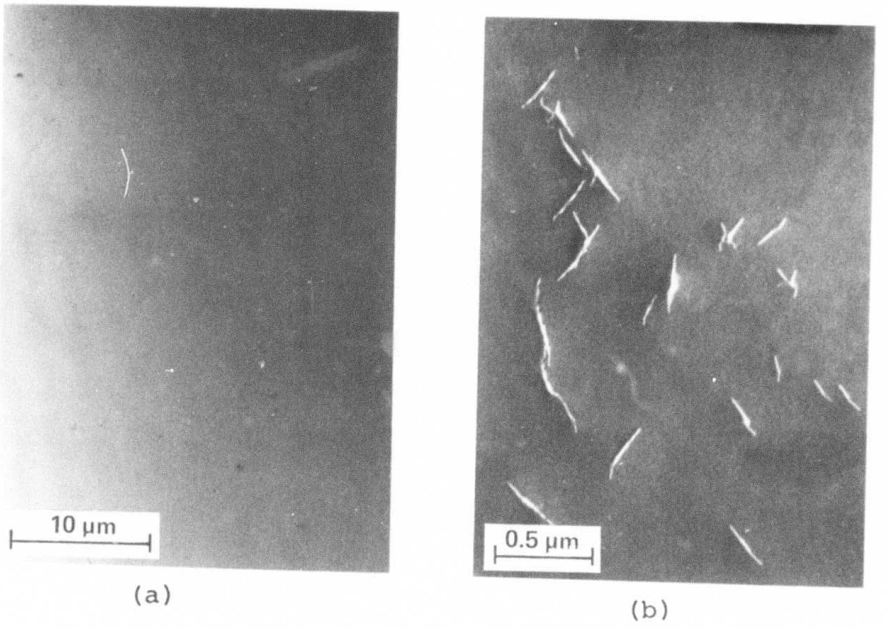

Fig. 9 TEM micrographs showing the crystal perfection of 10^{15} As/cm^2 implanted samples annealed with 180µm spot size. (a) 4.9, and (b) 3.4 joules/cm^2.

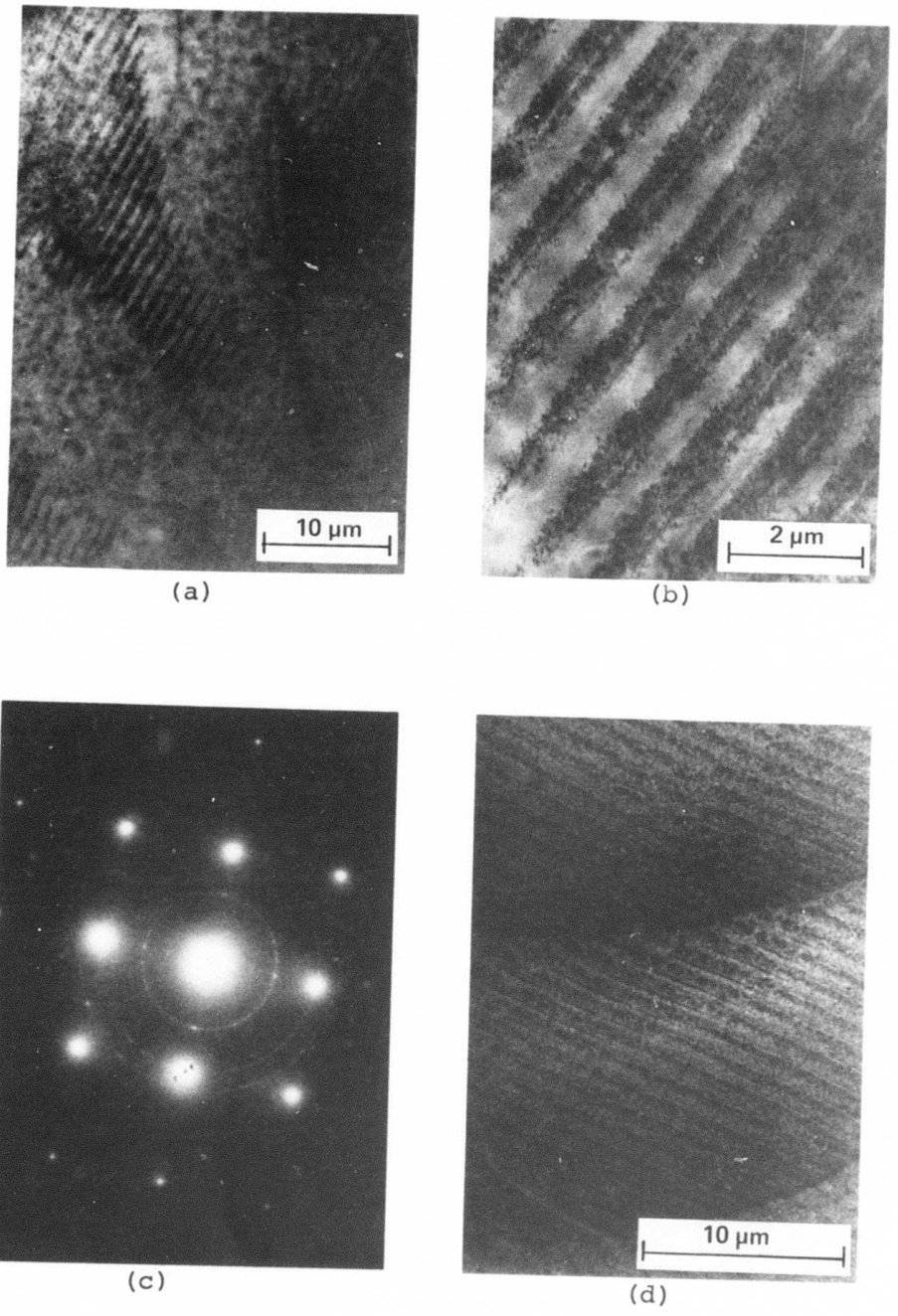

Fig. 10 TEM micrographs showing the crystal perfection of 10^{15} As/cm^2 implanted samples annealed with 180μm spot size. (a) and (b) 3.0 joules/cm^2, (c) electron diffraction pattern of (b), and (d) 2.4 joules/cm^2.

given in Fig. 10c. At 2.4 joules/cm , the entire annealed surface contains such a fringe structure, Fig. 10d. These data are summarized in Table VI.

From this investigation, it follows that the annealing threshold is very sensitive to the implantation dose. The threshold is about 2.2 joules/cm^2 for 10^{16} As^+/cm^2 implanted samples and 3.4 joules/cm^2 for 10^{15} As^+/cm^2 implanted samples. For annealing above the threshold, the implanted layer recrystallizes epitaxially; below the threshold, the annealed layer contains polycrystalline fringes spaced at 1.06 μm.

3.3.2 Annealing with 60 μm Spot Size

The annealing threshold depends also on the spot size of the laser beam. For 10^{16} As^+/cm^2 implanted samples, which are annealed with 60 μm spot size, the morphology of the annealed surface is shown in Figs. 11. The transition in surface morphology from the circular pattern which forms at high energy densities,(4.3 joules/cm^2 in Fig. 11a) to the periodic fringe structure which forms at low energy densities, (3.9 joules/cm^2 and 3.4 joules/cm^2, Figs. 11b), is essentially the same as obtained with the 180 μm spot size as shown in Fig. 6. It should be noted that the area of the annealed spots in Fig. 11 is smaller due to a smaller beam size. The spacing between two scans, Figs. 11a,b, is 10 μm. In Fig. 11c, the line spacing is 7.5 μm.

TABLE VI. Laser Annealing: Spot Size 180μm
Implantation: 80 KeV, As^+ $10^{15}/cm^2$

Energy joules/cm^2	Surface Morphology	Layer Perfection	Fig. No.
4.9	Smooth	Epi regrowth, defect-free	8a 9a
3.4* to 4.0	Smooth	Epi regrowth Dislocations	8b 9b
3.0	Fringe structure appears	Polycrystalline and single crystal area forming fringe structure	8c, 10a, 10b
2.4	Fringes cover surface	Poly-silicon in annealed area	8d, 10c

*Annealing threshold 3.4 joules/cm^2
Defect free epitaxial regrowth at 4.9 joules/cm^2

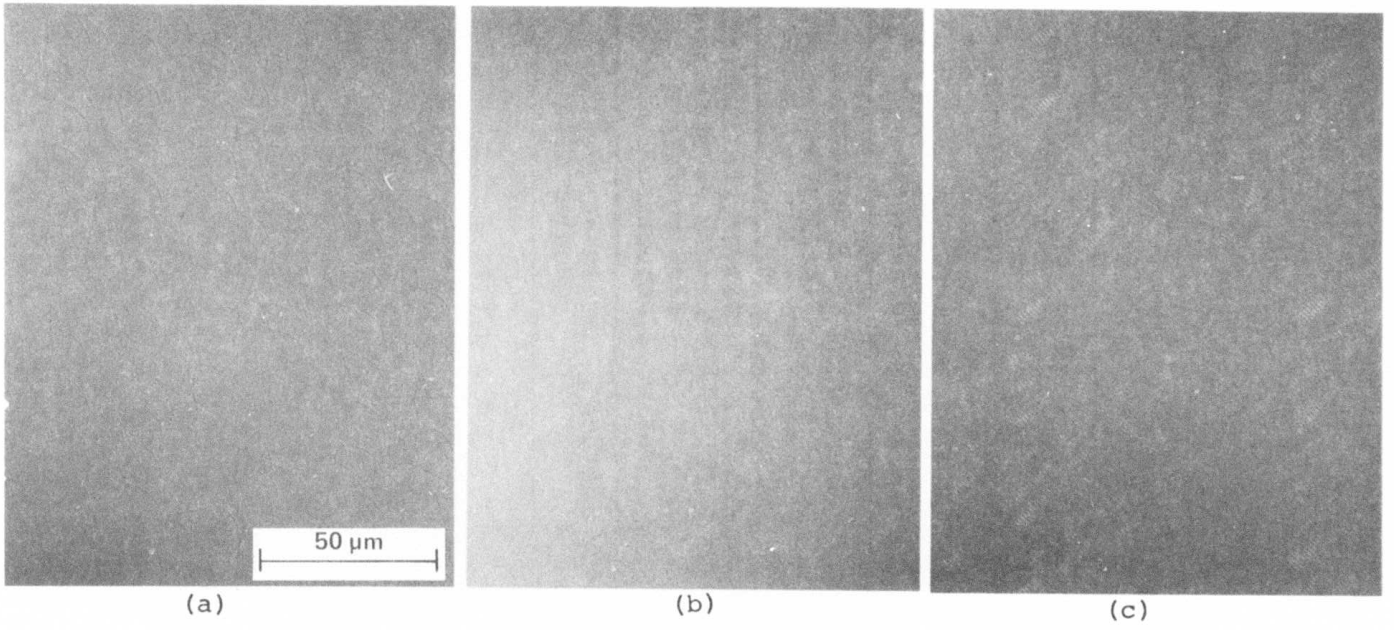

Fig. 11 Nomarski optical micrographs showing the surface morphology of 10^{16} As/cm^2 implanted samples annealed with 60µm spot size. (a) 4.3, (b) 3.9, and (c) 3.4 joules/cm^2.

TEM investigation indicate that at 4.3 joules/cm^2 the entire annealed layer recrystallizes into single crystal, Fig. 12a. The size of the recrystallized areas decreases as the energy density decreases. At 3.9 joules/cm^2, the periphery of the laser pulsed spot on the wafer remains polycrystalline, Fig. 12b. At 3.4 joules/cm^2, only the center of the pulsed spot recrystallizes, Fig. 12c. The annealing threshold is therefore taken as 3.4 joules/cm^2 for the 60 μm spot size, compared with 2.2 joules/cm^2 for the 180 μm spot size. This result indicates that a smaller spot size of the laser beam requires a higher annealing threshold.

10^{15} As^+/cm^2 implanted samples, annealed with a 60 μm spot, show no significant changes in surface morphology for an energy density between 5.2 joules/cm^2 and 3.9 joules/cm^2, Fig. 13a,b. For this range the annealed surface consists of a relatively ill-defined fringe structure at the periphery of the laser pulses. At 3.4 joules/cm^2, almost the entire surface is covered with such a structure, Fig. 13c.

TEM investigation shows that at 5.2 joules/cm^2, and 3.9 joules/cm^2, Figs. 14a,b, only the center of the annealed spot recrystallizes into single crystal while the periphery remains polycrystalline. This follows from the electron diffraction patterns shown in Figs. 14c,d. The single crystal (100) pattern, Fig. 14c, is obtained from the center of an annealed spot. The polycrystalline pattern shown in Fig. 14d results from the periphery of a spot. At

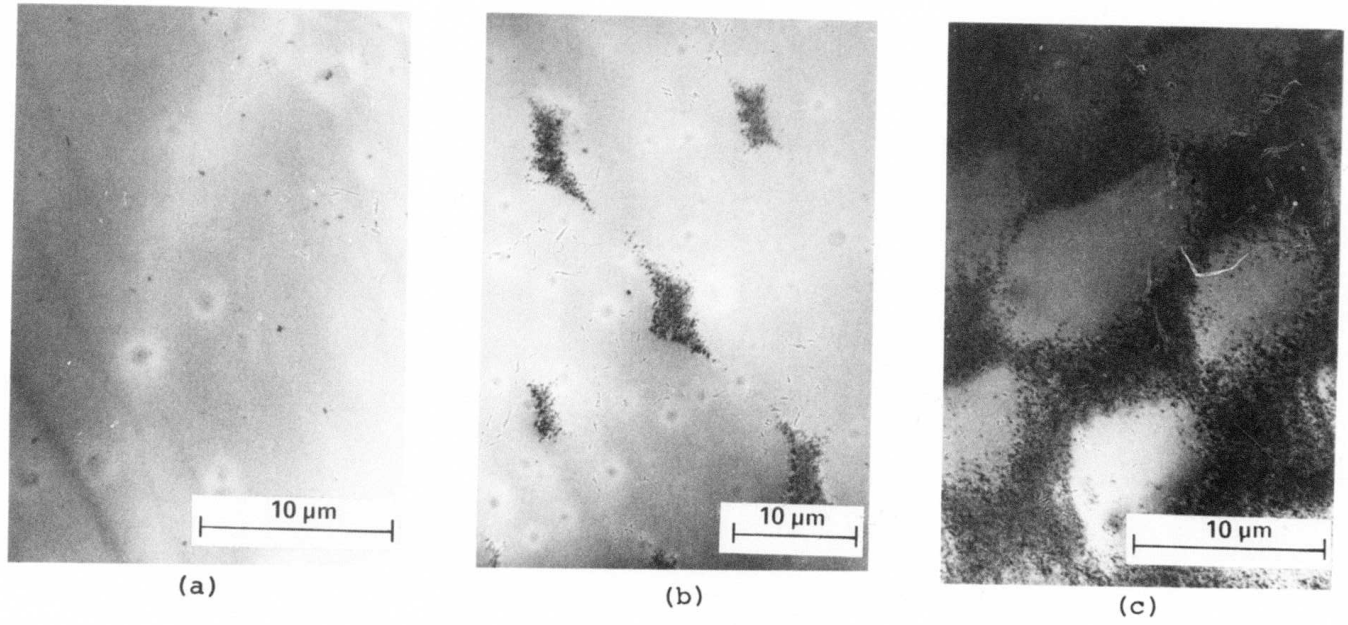

(a) (b) (c)

Fig. 12 TEM micrographs showing the crystal perfection of 10^{16} As/cm^2 implanted samples annealed with 60μm spot size. (a) 4.3, (b) 3.4 and (c) 3.4 joules/cm^2.

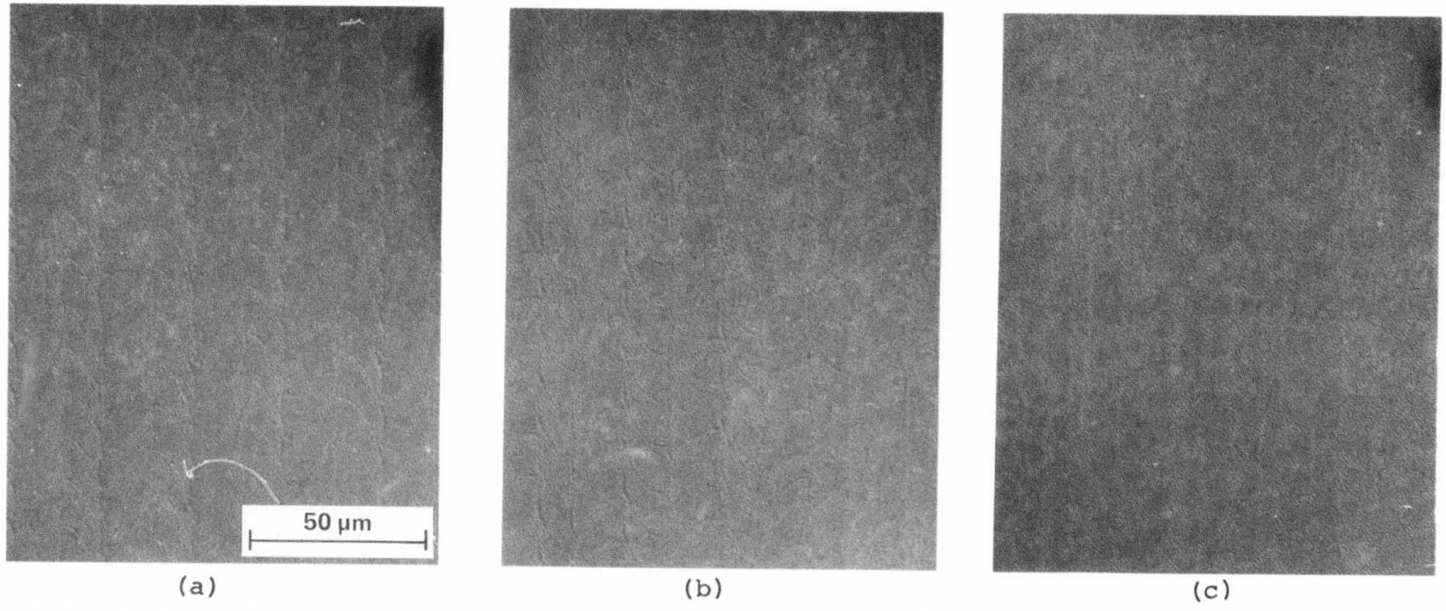

Fig. 13 Nomarski optical micrographs showing the surface morphology of 10^{15} As/cm^2 implanted samples annealed with 60µm spot size. (a) 5.2, (b) 3.9, and (c) 3.4 joules/cm^2.

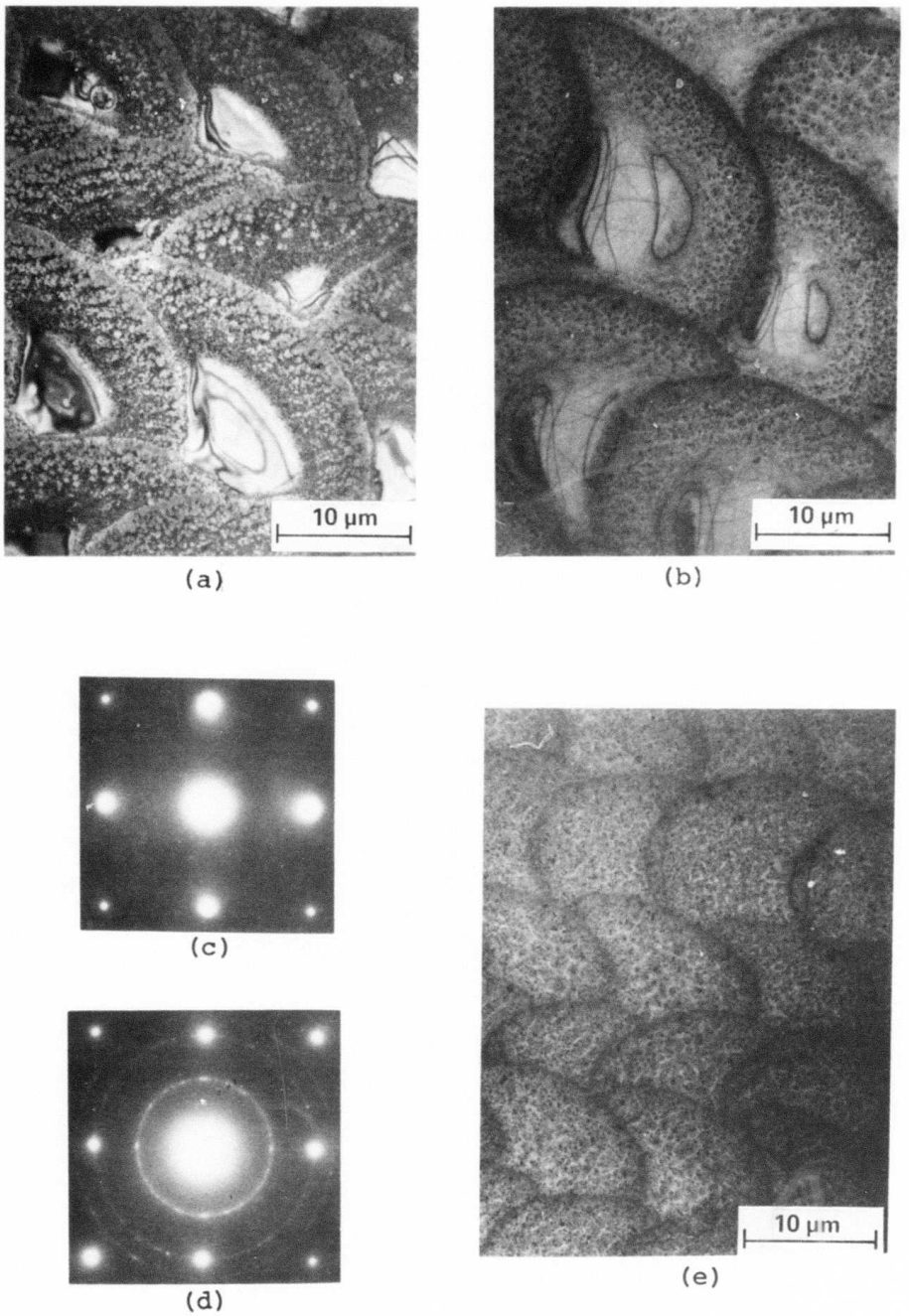

Fig. 14 TEM micrographs showing the crystal perfection of 10^{15} As/cm^2 implanted samples annealed with 60μm spot size. (a) 5.2, (b) 3.9 joules/cm^2, electron diffraction patterns taken from the center (c) and the periphery (d) of an annealed spot, and (e) 3.4 joules/cm^2.

3.4 joules/cm^2, laser annealing converts the implanted amorphous layer into a polycrystalline layer, Fig. 14e. This result shows that the annealing threshold for this case is higher than 5.2 joules/cm^2, compared with 3.4 joules/cm^2 found for the 180 μm spot size. This indicates again that the annealing threshold is higher for a smaller spot size of the laser beam. The variations in layer perfection obtained for different dopant concentrations and different laser power using a 60 μm large laser spot are summarized in Tables VII and VIII.

3.4 Junction Uniformity

Variations in junction depth occurring in laser annealed implanted layers are examined by the bevel-and-stain-technique. Figure 15 shows such a beveled and stained surface for a 10^{16}As/cm^2 implanted sample annealed with a 180 μm spot. The beveled surface shows an overlapping circular pattern which causes variations in junction depth. It can also be seen that the overlapping between two neighboring scans decreases with depth. The variation in impurity penetration between the center and the periphery of a laser pulse is approximately 0.07 μm. Such variations increase if the energy density in the beam decreases. This is the result of the smaller annealed spot size obtained for lower energies which in turn reduces the degreee of overlap between two neighboring scans.

TABLE VII. Laser Annealing: Spot Size 60μm
Implantation: 80KeV, As^+ $10^{16}/cm^2$

Energy joules/cm^2	Surface Morphology	Layer Perfection	Fig. No.
4.3	Smooth, circular pattern	Epi regrowth Defect free	11a 12a
3.9	Smooth, fringe structure around periphery of annealed spot	Large single crystal area in spot centers, polycrystalline around periphery	11b 12b
3.4*	Fringes extending toward center	Small single crystal area in spot center, rest polycrystalline	11c 12c

*Annealing threshold at 3.4 joules/cm^2
Defect free epitaxial regrowth at 4.3 joules/cm^2

TABLE VIII. Laser Annealing: Spot Size 60μm
Implantation: 80KeV, As^+ $10^{15}/cm^2$

Energy joules/cm^2	Surface Morphology	Layer Perfection	Fig. No.
5.2	Fringe Structure	Center of spot single crystal, periphery polycrystalline	13a 14a
3.9	Stronger fringes	Small single crystal area in center of spot large polycrystalline area around periphery	13b 14b
3.4	Fringes cover most of annealed surface	Annealed surface is polycrystalline	13c 14e

*Annealing threshold not determined but larger than 5.2 joules/cm^2
Defect free epitaxial regrowth not achieved.

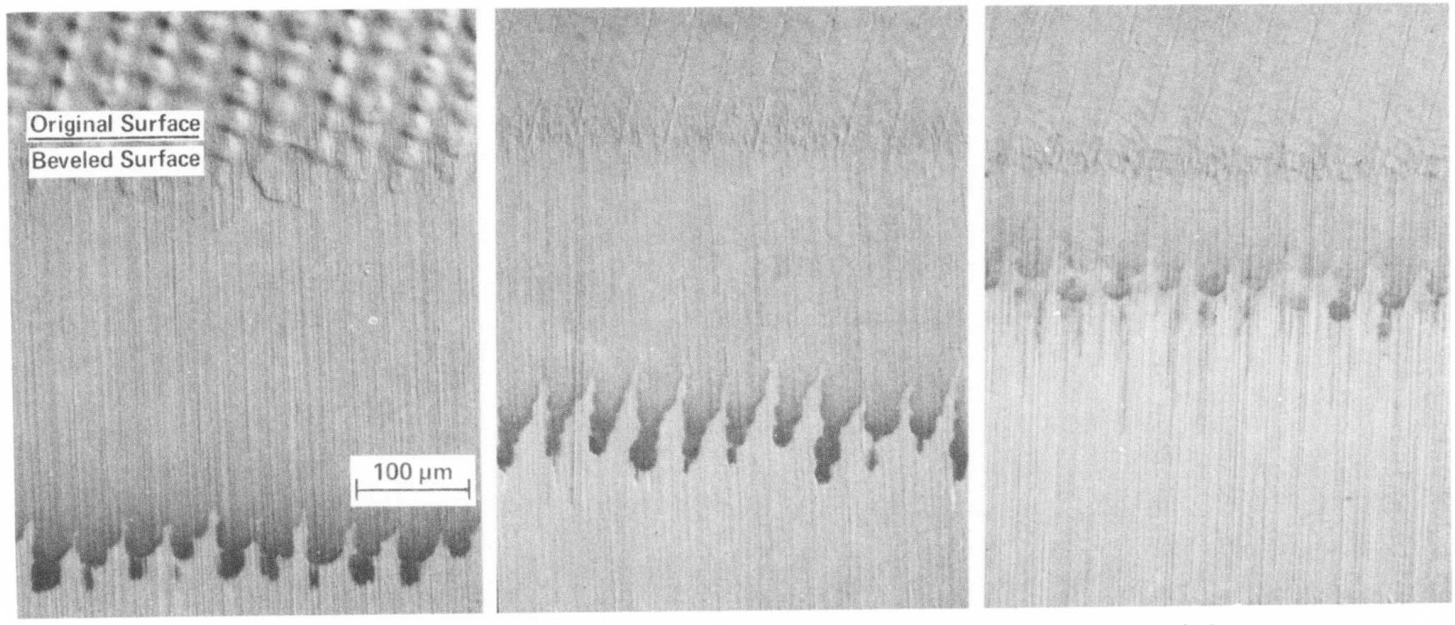

Fig. 15 Nomarski optical micrographs showing the stained, beveled surface of 10^{16} As/cm^2 implanted samples annealed with 180μm spot size. (a) 4.0, (b) 3.2, and (c) 2.4 joules/cm^2.

Similar observations are found for the 10^{15} As^+/cm^2 implanted samples annealed with a 180 μm spot size and for the 10^{16} As^+/cm^2 implanted samples annealed with a 60 μm spot. These results are shown in Figs. 16 and 17, respectively. The junction depth measured with the bevel-and-stain technique is given in Tables II, III, and IV. The junction depth measured by spreading resistance measurements and by He backscattering measurements compares favorably with the one obtained by the bevel-and-stain technique.

4.0 DISCUSSION

Arsenic implanted amorphous layers on silicon can be recrystallized into single crystal through laser annealing. Single crystal regrowth is achieved if the incident laser power is above a certain threshold. For proper annealing conditions it is found that practically all As atoms occupy substitutional sites in the recrystallized layer and thus are electrically active. Below the threshold, the implanted layer crystallizes polycrystalline and the As atoms are only partially electrically active.

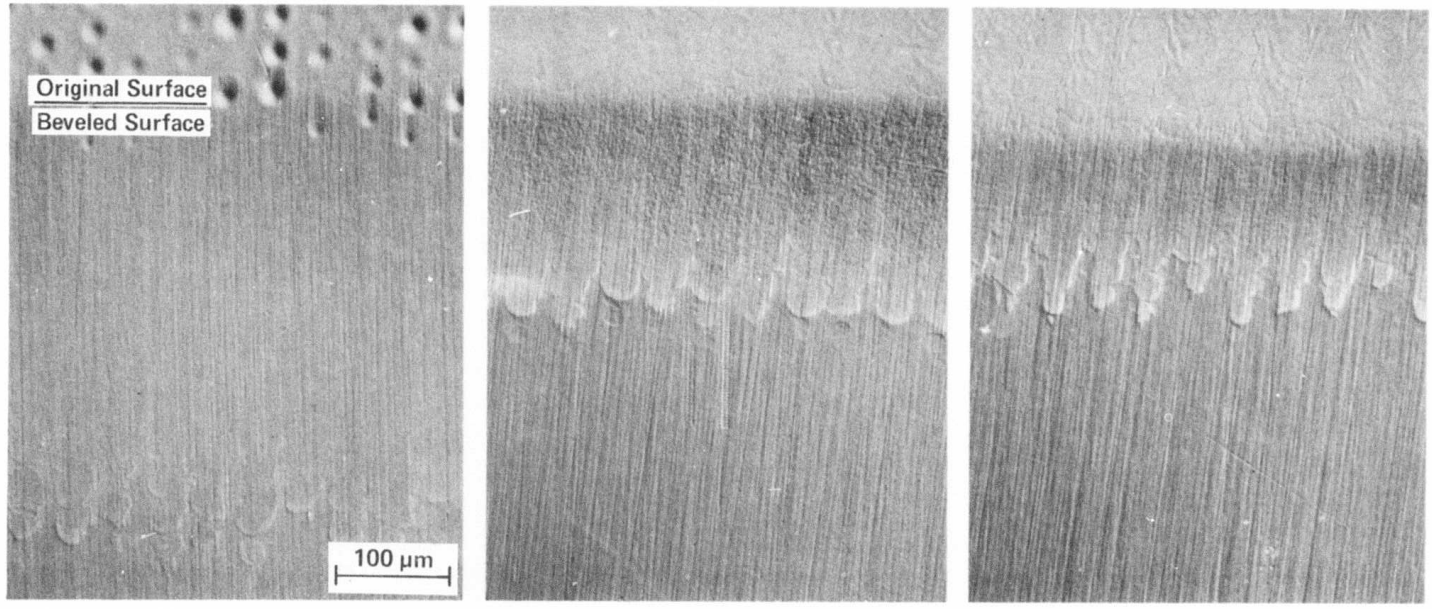

Fig. 16 Nomarski optical micrographs showing the stained, beveled surface of 10^{15} As/cm^2 implanted samples annealed with 180μm spot size. (a) 4.9, (b) 4.0 and (c) 3.4 joules/cm^2.

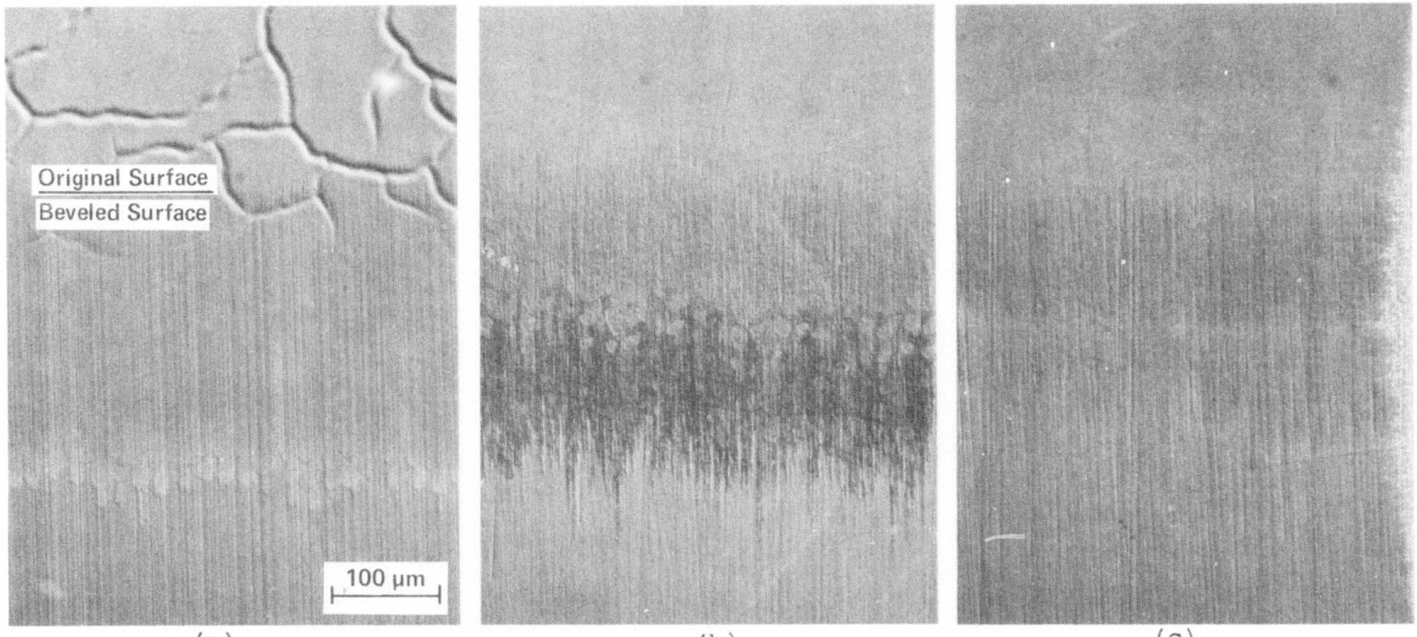

Fig. 17 Nomarski optical micrograph showing the stained, beveled surface of 10^{16} As/cm^2 implanted samples annealed with 60µm spot size. (a) 4.3, (b) 3.9, and (c) 3.4 joules/cm^2.

Doped recrystallized layers produced by laser annealing show good crystal perfection; however, junction uniformity obtained by this method can be variable. Variations in junction depth occur between and along laser scans. The junction depth variations along the annealing scans result mainly from energy instabilities of laser pulses. The variation in junction depth between the laser scans is caused by the non-uniform temperature distribution in a laser spot. The distribution of energy density in a TEM_{00} mode laser spot follows a Gaussian distribution. The annealed layer undergoes structural changes according to this temperature distribution. This is shown schematically in Fig. 18. The crystallized area in an annealed spot is given by the circle with radius r_c. In this area the beam temperature is T_c and high enough to crystallize the amorphous silicon. The polycrystalline area is located between the two circles with radius r_c and r_a. For this area the beam temperature is too low. Similar results are reported by Bean, et al (9). Through proper overlapping between two consecutive laser pulses, the entire annealed surface can be converted into single crystal, provided that the temperature generated by the second pulse is sufficient to crystallize the area which remained polycrystalline after the first pulse.

Although single crystal perfection in laser annealed layers can be achieved, problems exist with the impurity profile

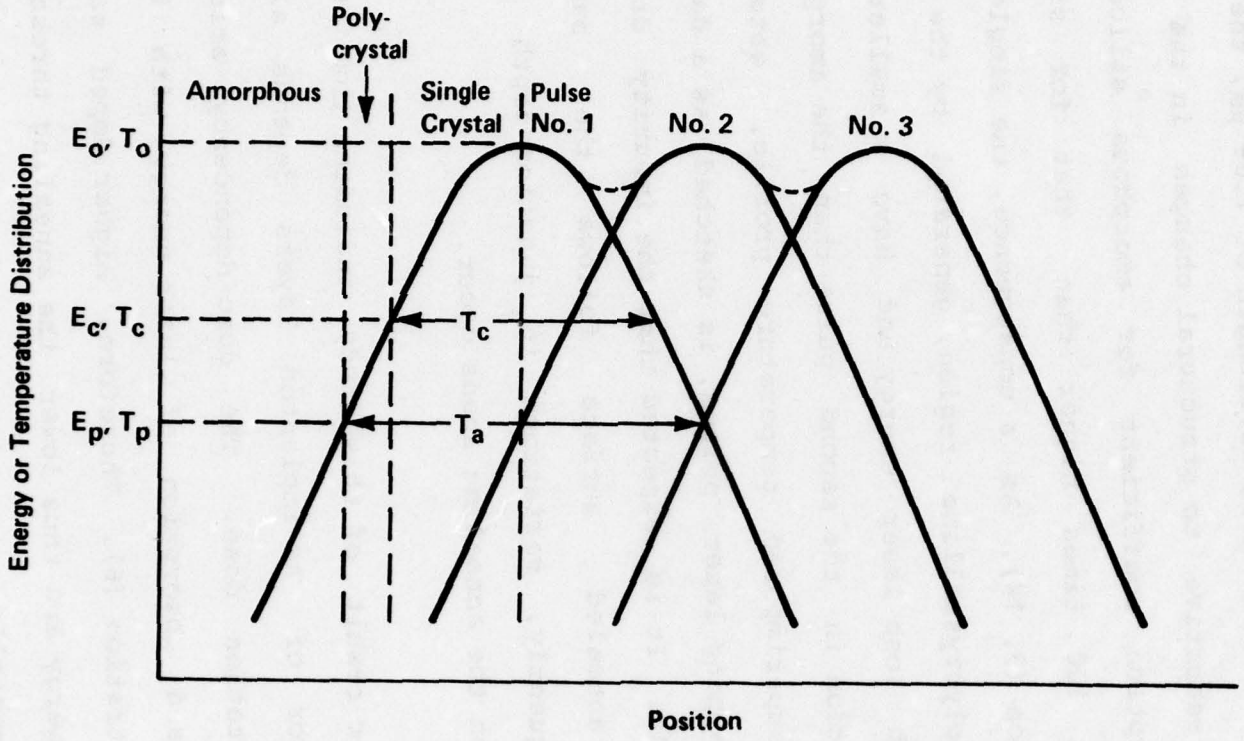

Fig. 18 Schematic drawing of energy or temperature distribution in a laser annealed spot.

produced by this technique. The dopant distribution is essentially controlled through the temperature profile of the overlapping pulses. The temperature profile is determined by the absorption of laser energy in the silicon. At the Nd:YAG laser wavelength of 1.06 μm, the absorption is very sensitive to structural changes in the silicon. The absorption coefficient for amorphous silicon (9, 13) is about 100 times higher than that for single crystal silicon (9, 14). As a consequence, the single crystal and the polycrystalline region, generated by the first pulse, absorb less laser energy and have a smaller temperature elevation in the second pulse than the amorphous region. The superimposed temperature profile, obtained by two overlapping laser pulses, is sketched as a dashed line in Fig. 18. It is expected that the impurity distribution in the annealed surface follows the same pattern. Consequently, variations in junction depth in the area between the annealing scans occur.

Another result of this study indicates that the annealing behavior of As-implanted layers depends also on the implantation dose. The dose dependency arises from an increased absorption of laser energy with increased As concentration (6). Therefore, higher doped samples absorb more energy and thus lower the annealing threshold as found experimentally.

The dependency of the annealing behavior on the spot size of the laser beam can be understood if one considers the temperature profile of the annealing laser spot. The temperature profile in the surface of an annealed spot follows a Gaussian distribution and can be expressed as:

$$T = T_0 \exp\left(-\frac{r^2}{2r_o^2}\right)$$

where T_0 is the peak temperature at r=0, and r_o is the 1/e spot size of laser beam. From this equation the temperature gradient at a recrystallized spot r can be expressed as:

$$\frac{dT}{dr} = T_c \left(-\frac{r_c}{r_0^2}\right)$$

Because T_c, the temperature required for recrystallization, is independent of the 1/e spot size r_o, the temperature gradient at r_c is proportional to $(-r_c/r_o^2)$. The value of r_c is about 50 ~ 70 µm for the 180 µm spot size, and 10 ~ 20 µm for the 60 µm spot size as given in Table I. As a result, the temperature gradient is about 2 to 3 times higher for the 60 µm spot size. The high temperature gradient for the 60 µm spot size is evident from the Figs. 12 and 14 compared with the Figs. 7, 9 and 10. Fig. 14 indicates also that due to the high temperature gradient of the 60 µm spot size and the lower absorption for the 10^{15} As/cm^2 implanted samples, the polycrystalline periphery cannot be converted into single crystal by

overlapping. As a result, the implanted As atoms are only partially activated electrically. It follows also that the high-temperature gradient leads to poor junction uniformity.

5.0 CONCLUSIONS

The electrical activity of implanted As atoms after laser annealing depends on the crystal perfection achieved in the laser annealed implanted layer. At and above the annealing threshold, the implanted amorphous layer crystallizes into a layer of single crystal through epitaxial regrowth. In the crystallized layer, almost all As atoms occupy substitutional silicon lattice sites and are electrically active. For annealing below the threshold, the implanted layer is polycrystalline, and the implanted As atoms are only partially electrically active.

Junction uniformity in laser annealed samples can vary. The variation in junction uniformity arises from the non-uniform distribution of energy in a laser beam. The energy distribution in the beam determines the temperature profile and thus the impurity distribution in the annealed layer. The temperature gradient caused by the temperature profile of the laser spot is smaller for larger spot size. As a result, annealed layers show better crystal perfection and better junction uniformity for larger spot sizes.

6.0 ACKNOWLEDGMENTS

He^4 backscattering measurements were performed by Dr. W. K. Chu. Spreading resistance measurements were made by Mr. E. F. Gorey.

7.0 REFERENCES

1. A. Gat and J. F. Gibbons, T. J. Magee, P. Peng, V. R. DeLine, P. Williams, and C. A. Evans, Jr., Appl. Phys. Letters, 32, 276 (1978).

2. J. S. Williams, W. L. Brown, H. J. Leamy, J. M. Poate, J. W. Rodgers, D. Rousseau, G. A. Rozgonyi, J. A. Schelnutt, and T. T. Sheng, Appl. Phys. Letters, 33, 542 (1978).

3. D. H. Auston, J. A. Golovchenko, P. R. Smith, C. M. Surko and T. N. C. Venkatesan, Appl. Phys. Letters, 33, 539 (1978).

4. R. T. Young, C. W. White, G. J. Clark, J. Narayan, W. H. Christie, M. Murakami, P. W. King, and S. D. Kramer, Appl. Phys. Letters, 32, 139 (1978).

5. H. J. Leamy, G. A. Rozgonyi, T. T. Sheng, and G. K. Celler, Appl. Phys. Letters, 32, 535 (1978).

6. T. N. C. Venkatesan, J. A. Golovchenko, J. M. Poate, P. Cowan, and G. K. Celler, Appl. Phys. Letters, 33, 429 (1978).

7. C. W. White, W. H. Christie, B. R. Appleton, S. R. Wilson, P. P. Pronko, and C. M. Magee, Appl. Phys. Letters, 33, 663 (1978).

8. M. von Allmen, W. Luthy, and K. Affolter, Appl. Phys. Letters, 33, 824 (1978).

9. J. C. Bean, H. J. Leamy, J. M. Poate, G. A. Rozgonyi, J. P. van der Ziel, and G. K. Celler, J. Appl. Phys. 50, 881 (1979).

10. G. K. Celler, J. M. Poate, and L. C. Kimerling, Appl. Phys. Letters, 32, 464 (1978).

11. B. J. Masters, Proceedings of "Laser Effects in Ion Implanted Semiconductors," Ed. by E. Rimini, Catania, Universita di Catania, Corso, Italia, August 31, 1978.

12. W. S. Johnson and J. F. Gibbons, "Projected Range Statistics in Semiconductors," Stanford University (1970).

13. G. N. Maracas, G. L. Harris, C. A. Lee and R. A. McFarlane, Appl. Phys. Letters, 33, 453 (1978).

14. G. K. M. Thutupalli and S. G. Tomlin, J. Phys. C, Solid State Phys., 10, 467 (1977).

15. G. G. MacFarlane, T. P. McLean, J. E. Quarrington, and V. Roberts, Phys. Rev., 111, 1245 (1958).

CHAPTER II

MINORITY CARRIER LIFETIME IMPROVEMENT IN SILICON THROUGH LASER DAMAGE GETTERING

MINORITY CARRIER LIFETIME IMPROVEMENT IN SILICON THROUGH LASER DAMAGE GETTERING

1.0 INTRODUCTION

Controlled mechanical damage produced on silicon wafer backsides has been used successfully to improve minority carrier lifetime distributions on the device side of a silicon wafer. Several techniques are described in the literature to produce such damage including mechanically grinding (1), impact sound stressing (ISS) (2), and ion implantation (3,4). Mechanical damage gettering relies on the dislocations generated during heat processing of a silicon wafer and is quite effective as long as the dislocations generated are confined to the backside of the silicon wafer and do not slip to the frontside. This is achieved for mechanical damage produced by ISS or ion implantation. Both techniques maintain excellent control over the damage introduced. Abrasive techniques, such as grinding, have problems in controlling the introduction of damage into the silicon surface.

This report describes a new technique to introduce well controlled damage into a silicon surface. The damage is easily produced through incident laser radiation. The advantage of this technique is that it can be effectively

integrated into a semiconductor processing line. The damage can be introduced at any desired processing step and multiple applications are also possible. The following presents a detailed account of this technique.

2.0 EXPERIMENTAL

In this investigation, boron-doped, 2Ω-cm, (100) oriented silicon wafers of low oxygen content to avoid internal gettering are used. Half of the backsides of the wafers are damaged through a Q-switched Nd:YAG laser beam operated at a wavelength of 1.06 μm. The damage is arranged in a pattern of parallel scan lines at constant spacing. The laser is operated under different power conditions to produce different damage depths in the wafer between 0.3 to 20 μm. This is achieved by changing the energy density in the beam which can be adjusted through use of different objective lenses. For a damage depth of approximately 18 to 22 μm, a 27 mm objective lens is used. For such a lens the 1/e spot size of the laser beam is 65 μm, the energy density is 33.2 joules/cm^2 and the scan speed used is 15.2 cm/sec. For a damage depth below 10 μm, a 48 mm objective lens is used. For this lens the 1/e spot size is 115 μm, the energy density varies from 5 to 15 joules/cm^2, and the scan speed used is 25.4 cm/sec. Additional changes in laser power output can be achieved through varying the pulse rates.

The line spacing determines the number of damage sites produced in the wafer per unit area. The spacings investigated range from 0.5 to 5 mm.

The effectiveness of laser gettering is evaluated as a function of multiple oxidations. Minority carrier lifetime is used as a wafer quality monitor and is measured after each oxidation step. Such measurements are made for up to three oxidation cycles.

After laser damaging, the wafers are processed for fabrication of MOS capacitors. First they are cleaned in NH_4-H_2O_2, HCℓ-H_2O_2, and HF solutions. Subsequently, a 5000Å thick oxide is grown at 1000°C using a dry-wet-dry oxidation cycle. Finally, 1.5 mm dots are deposited on the wafer frontside. A sintering step (for good ohmic contact) is made in forming gas at 400°C for 30 minutes.

The minority carrier lifetime in silicon is measured using the MOS capacitors. The lifetime is determined from the C-t transient response of the MOS devices (5). The effectiveness of laser damage gettering is evaluated by comparing the lifetimes obtained in the wafer halves which are laser damaged versus the non-damaged halves.

The crystallographic characteristics of laser damage in silicon are analyzed by transmission x-ray topography and

transmission electron microscopy (TEM). X-ray topographs are recorded with MoK_{α} radiation. Samples for TEM investigations are prepared by jet etching. The samples are examined in a JEOL microscope operated at 200 keV. The depth of laser damage is measured using bevel techniques combined with Sirtl etching of the beveled surfaces.

3.0 RESULTS

3.1 Damage Characterization

3.1.1 Damage Morphology

The photomicrographs presented in Figs. 1 show the morphology of silicon surfaces laser damaged using different energy densities. At 5.3 joules/cm^2, the surface consists of overlapping circular patterns (Fig. 1a). As the energy density increases to 6.5 joules/cm^2, the center of the laser pulse pattern on the wafer forms a depression and the damage pattern is much more pronounced, Fig. 1b. This result illustrates that below 6.5 joules/cm^2, the laser interaction with the silicon surface results in localized melting of the surface. At 8.2 joules/cm^2, laser interaction with the surface results in silicon evaporation. As a consequence, the damaged surface shows a groove, Fig. 1c. The depth of the groove increases with the laser power applied.

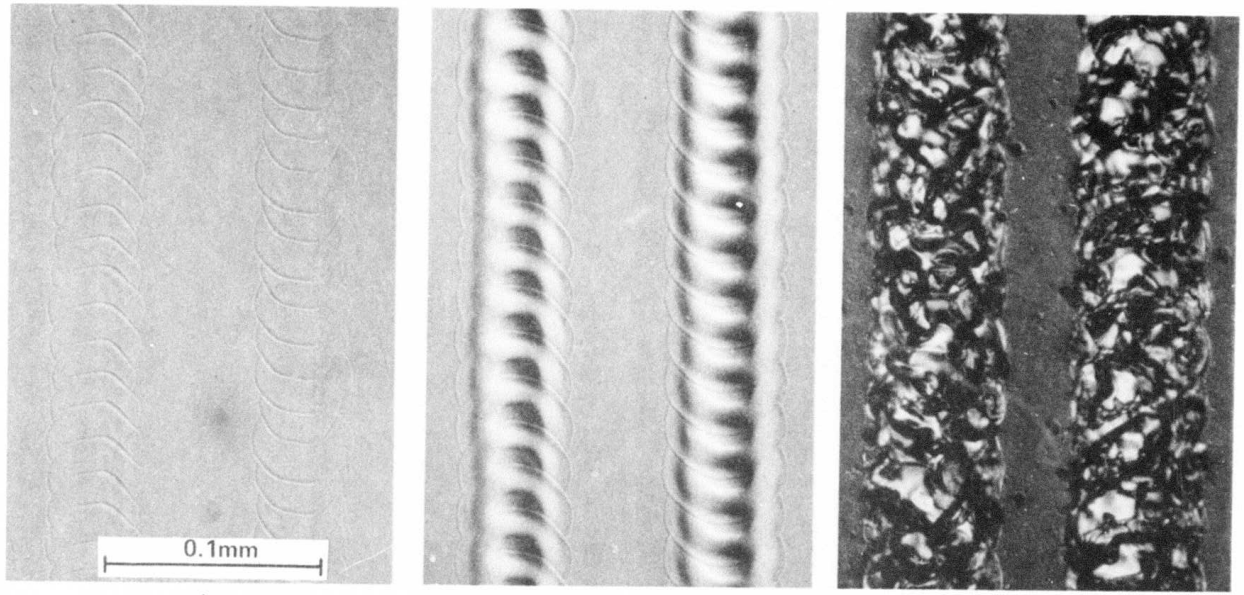

Fig. 1 Optical micrographs showing the morphology of laser damaged silicon surface. (a) 5.3, (b) 6.5, and (c) 8.2 joules/cm^2.

3.1.2 Damage Depth Measurements

The depth of laser damage in silicon is measured on a Sirtl etched beveled surface. Such surfaces corresponding to Figs. 1 are shown in Fig. 2. It can be seen that the damage depth increases with the laser energy density. Note that the bevel angle used for Figs. 2b and 2c is larger than the one used for Fig. 2a. The measurements of damage depth as a function of energy density are plotted in Fig. 3. Figure 3 shows that below 7 joules/cm^2 and above 8 joules/cm^2, the damage depth increases almost linearly with the power application. Between 7 and 8 joules/cm^2 a transition occurs which causes a steep increase in damage depth. As shown in Figs. 1, the laser damage below 7 joules/cm^2, involves primarily surface melting while above 8 joules/cm^2 silicon evaporates. The sharp increase in damage depth between 7 and 8 joules/cm^2 is associated with the transition from melt formation to vapor formation that occurs at this power level.

3.1.3 Damage Analysis

The crystal imperfections generated in the silicon through the laser impact are examined through x-ray topography and transmission electron microscopy (TEM). X-ray topographs recorded of silicon wafers exposed to a laser energy below 7 joules/cm^2, do not reveal any damage contrast. Silicon

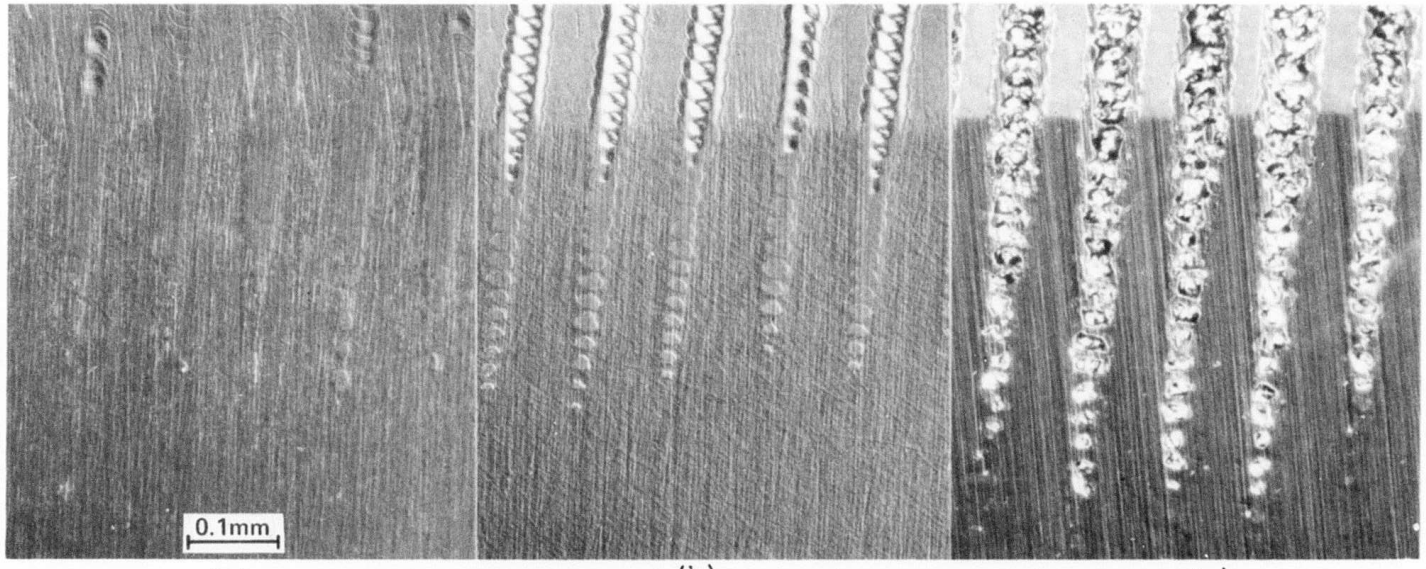

Fig. 2 Optical micrographs showing the depth of laser damage in silicon.

(a) 5.3 joules/cm^2, bevel angle 4.17',
(b) 6.5 joules/cm^2, bevel angle 15.0', and
(c) 8.2 joules/cm^2, bevel angle 34.3'.

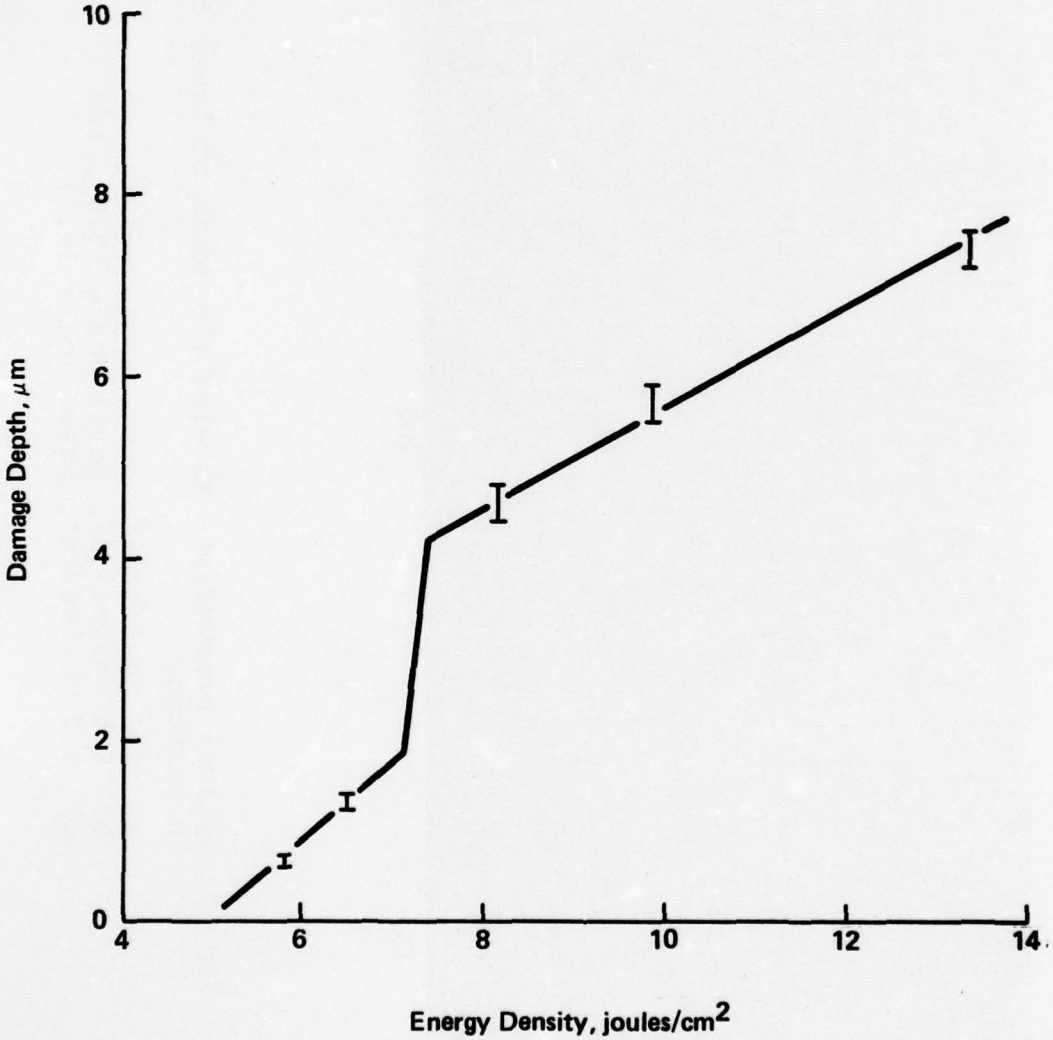

Fig. 3 The depth of laser damage in silicon as a function of energy density.

wafers exposed to energies of 8 joules/cm^2 or larger clearly show damage contrast in x-ray topographs. The x-ray topograph shown in Fig. 4a represents a wafer in which half of the wafer was laser damaged at 8.2 joules/cm^2 with a 1.00 mm line spacing. The corresponding section topographs for the laser-damaged half and the non-damaged half are shown in Figs. 4b and 4c.

3.1.3.1 TEM Analysis Before Oxidation

TEM investigations confirm that below the transition threshold, indicated in Fig. 3, laser action causes only surface melting. The solidified surface after melting is defined by a surface ripple at the periphery of the laser pulse pattern. An example is shown in Fig. 5a. The melted surface recrystallizes through epitaxial regrowth. As a result, no crystal defects are generated. The height of the surface ripple is about 0.25 times the extinction length of the electrons in silicon. Using the <220> diffraction at 200 keV, the height ripple is estimated to be approximately 500Å. This height decreases as the energy density decreases. Oxidation of such a surface does not produce any significant structural damage in the wafer. This is shown in Fig. 5b.

Above the transition threshold, laser interaction with the silicon leads to the evaporation of silicon. The laser

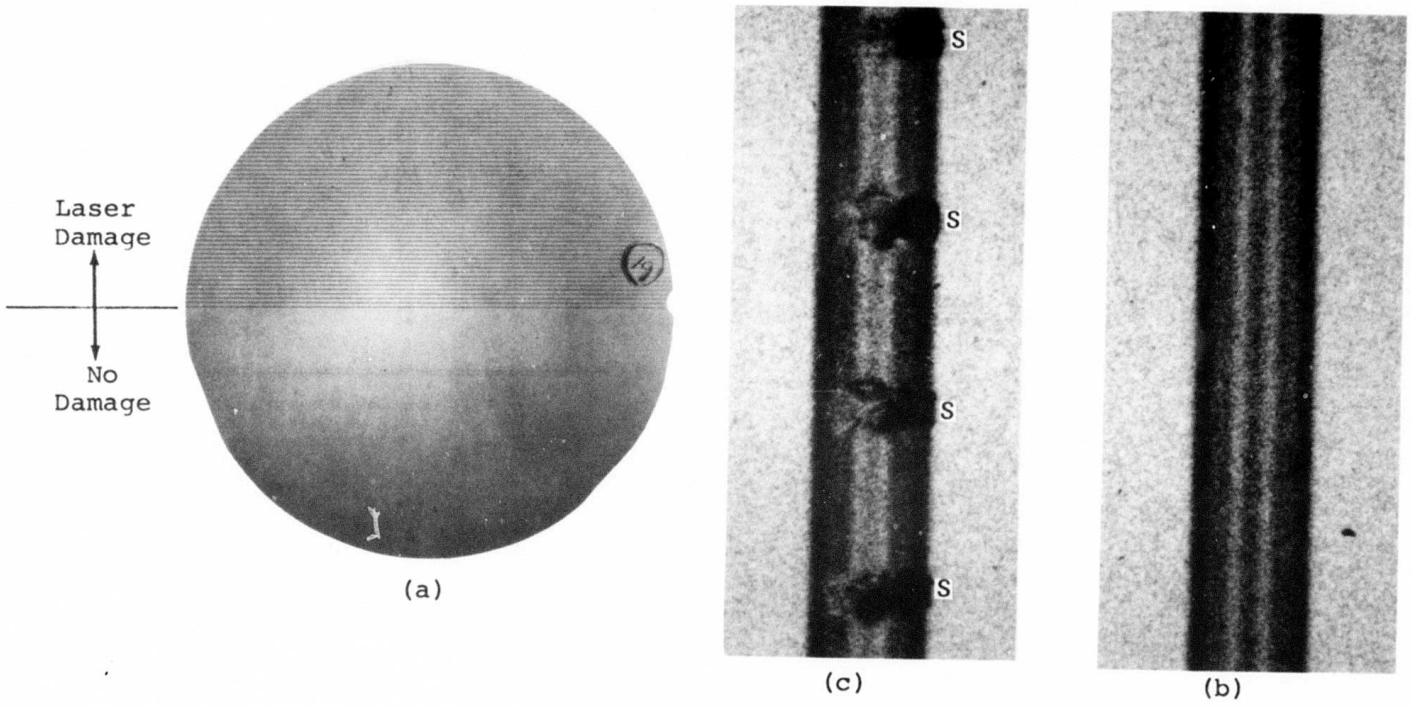

Fig. 4 (a) Transmission x-ray topograph showing half of a wafer laser damaged at 8.2 joules/cm^2 and 0.5mm line spacing. The corresponding section topographs for the laser damaged half (b), and for the non-damaged half (c). S refers to damage center.

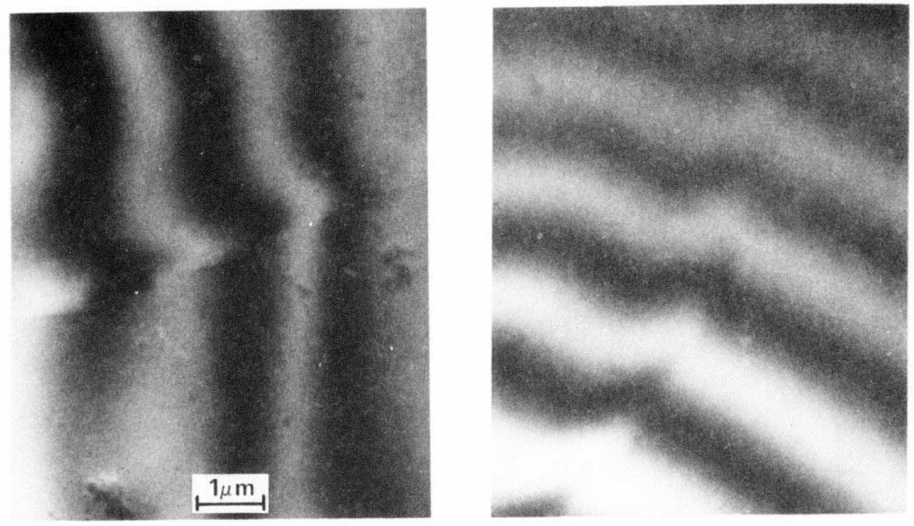

Fig. 5 TEM micrographs showing a remelt surface laser damaged at 6.5 joules/cm^2. (a) as damaged, (b) after oxidation.

action is so vigorous that the crystal perfection of silicon is locally destroyed. Several different crystal defects are observed after laser impact. At the center of a laser pulse pattern frequently polycrystalline grains are found, Fig. 6a. The formation of such polycrystalline grains indicates that for large incident laser power, which results in silicon evaporation rather than silicon melt formation, epitaxial regrowth, as observed after melt formation, does not occur. The recrystallized grains are found to be misoriented with respect to the underlying substrate. At the periphery of the laser pulse, scratch-like damage, dislocations and stacking faults are found. This is shown in Figs. 6b and 6c. The scratch-like damage results from uneven local laser heating. There is evidence that the dislocations and stacking faults originate from this type of damage. This is shown in Fig. 7 where dislocations are initiated at such damage sites, at position S. These dislocations relieve the strain fields which result from the non-uniform local heating. Many times dislocations are found to disassociate into stacking faults as shown at position F, in Fig. 7. Contrast analysis of photomicrographs as shown in Fig. 7a and 7b indicates that the faults are bound by Shockley partial dislocations. Stacking fault formation is energetically unfavorable for increasing fault size. This leads to the formation of total dislocations. In addition to these defects, the laser-damaged area is highly strained. This follows from

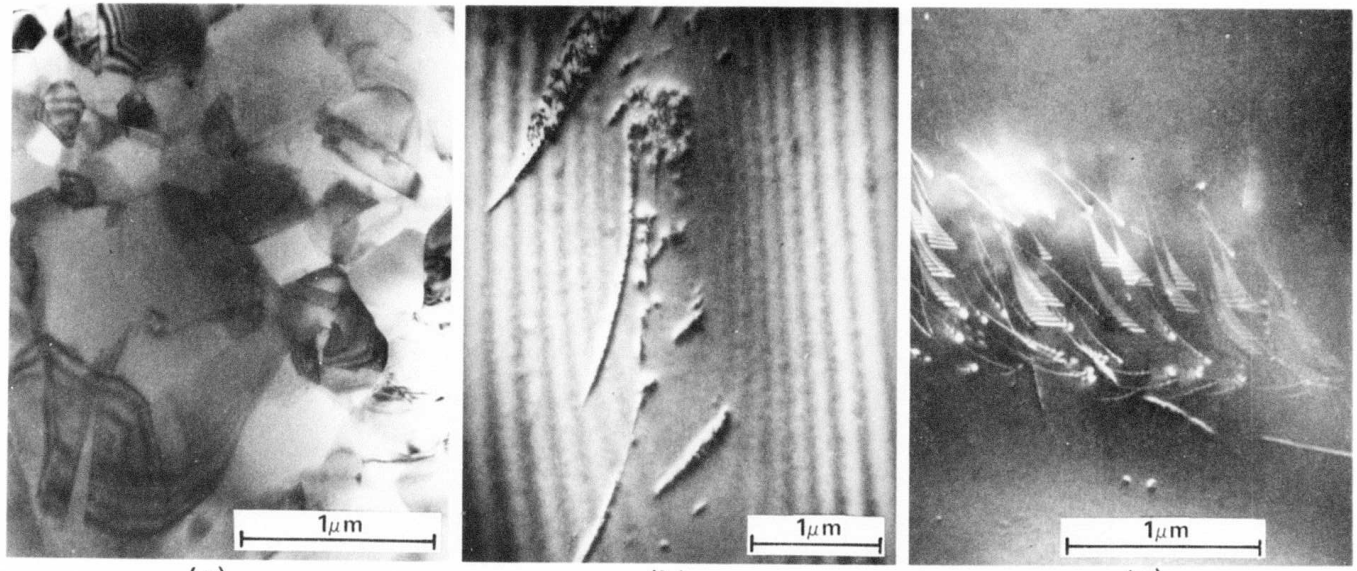

(a) (b) (c)

Fig. 6 TEM micrographs showing three characteristic types of crystal defects generated by laser damaged at 8.2 joules/cm^2 and above. (a) polycrystalline grains, (b) scratch-like damage, and (c) dislocations and stacking faults.

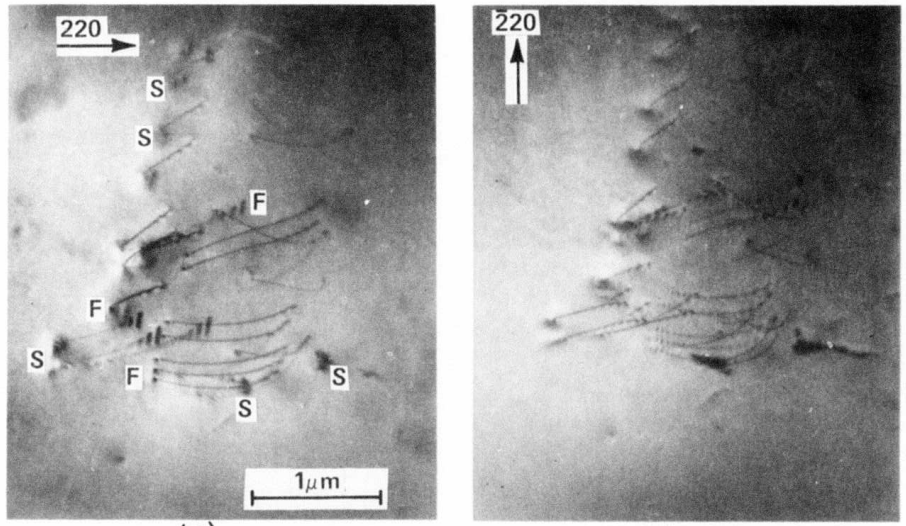

Fig. 7 TEM micrographs showing dislocations and stacking faults originating from scratch-like damage, S. (a) g=$\bar{2}20$, (b) g=220. The faults are out of contrast in (b).

diffraction image shifts observed in transmission electron micrographs and also from section x-ray topographs, Fig. 4b.

3.1.3.2 TEM Analysis After Oxidation

After a first oxidation, dislocations are the dominant crystal defects in the laser damaged area. The dislocations originate from several sources. Figure 8 shows that interfaces of misoriented recrystallized grains can generate dislocations. Another source is the scratch-like damage. This is shown in Fig. 8b where dislocations originate at position S. A third source is the strained areas which generate a high density of dislocation loops. The generation of these loops is associated with the relief of the strain introduced by the laser damage.

The most active dislocation source is the interface between misoriented grains. Dislocations generated at such interfaces glide in a (111) plane with a a/2<110> Burgers vector inclined to the (100) surface. The dislocations are half loops. The two ends of such a half loop tend to be anchored at the grain interface. The density of the loops and the distance of the dislocation movement from the grain interface increases with the laser power applied. At a power of 33.3 joules/cm^2, which generates a damage depth of 20 μm, such half loops can be seen in x-ray topographs. This is shown in Fig. 9. As the loops glide, their ends are

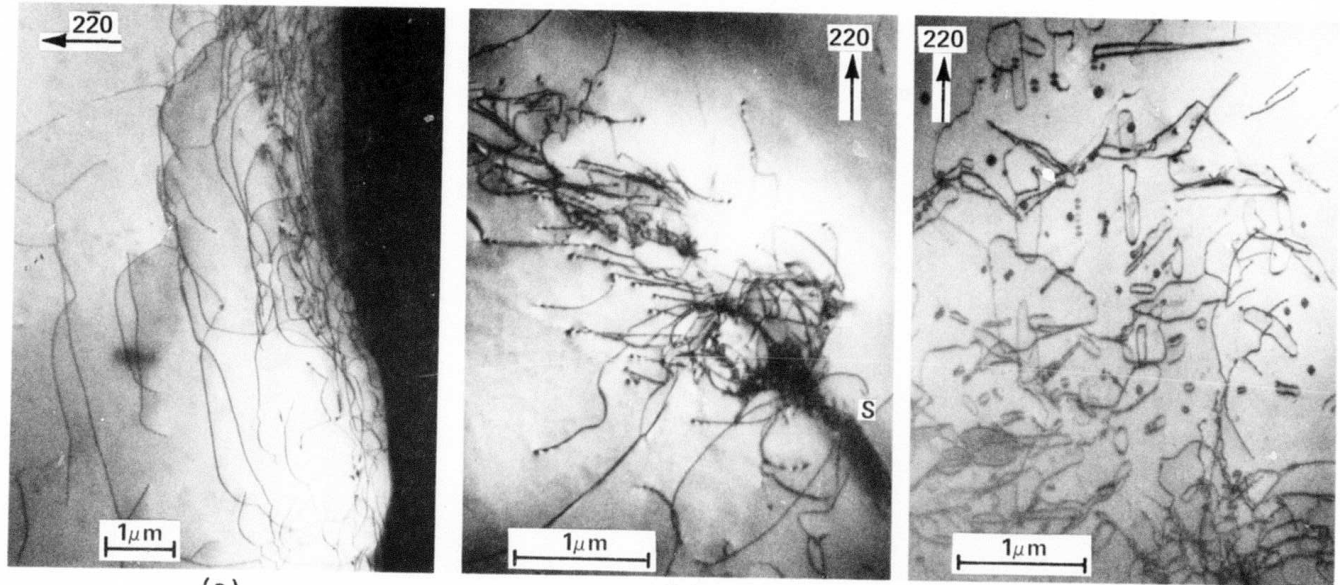

Fig. 8 TEM micrographs showing that after a first oxidation, dislocations originate from three main sources. (a) the interface of a misoriented recrystallized grain, (b) scratch-like damage, S and (c) strain fields introduced by laser damage.

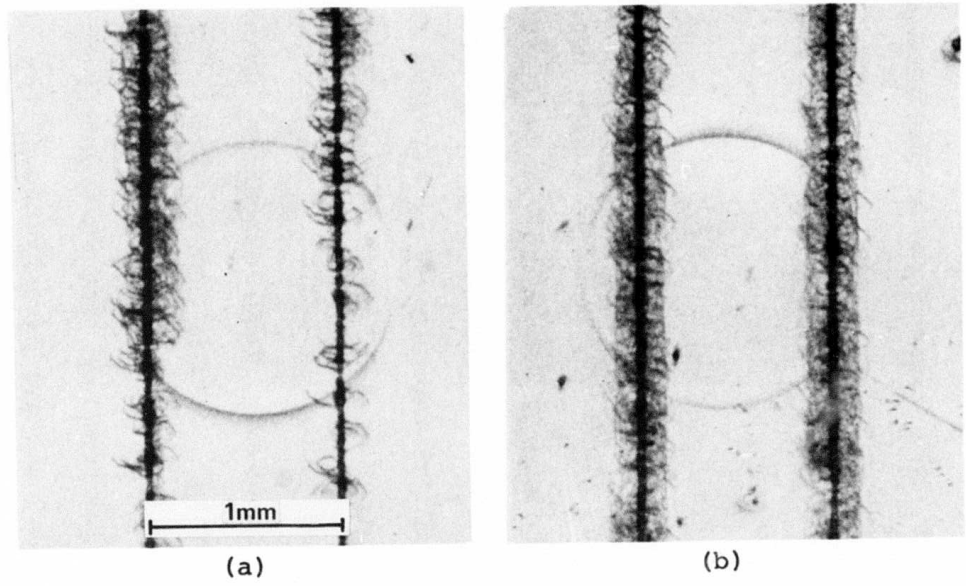

Fig. 9 Transmission x-ray topographs of (a) and (b) showing that after a first oxidation, dislocations and dislocation half loops originate from highly damaged scan lines. The energy density used is 33.3 joules/cm^2 and the damage depth is about 20μm. The line spacing is 1 mm. The circular pattern is a 1.5 mm MOS capacitor.

released from the laser damaged area and propagate into the undamaged substrate. Additional high temperature processing causes dislocation multiplication, movement and interaction.

3.2 Laser Damage Gettering

Laser gettering is investigated as a function of damage depth, line spacing, and multiple oxidations. Lifetime values are obtained from MOS capacitors as described in Section 2 of this report.

The effectiveness of laser gettering as a function of laser energy density is given in Table I. The damage depth corresponding to the energy densities listed in Table I are shown in Fig. 2. Table I indicates that after the first oxidation, a significant improvement in lifetime is achieved for an energy density of 8.2 and 9.9 joules/cm^2. In the absence of internal gettering centers smaller improvements in lifetime are observed using an energy density below 6.5 joules/cm^2. This result shows that for maximum gettering efficiency, a certain amount of damage must be generated in wafers free of internal gettering centers. This occurs for an energy density above the threshold, indicated in Fig. 3. To substantiate these findings, wafers #5 through #10 (Table I) previously damaged at 6.5 and 5.3 joules/cm^2 were redamaged at 11.2 joules/cm^2. It can be noted that after a second oxidation of these wafers,

TABLE I. The Effectiveness of Laser Gettering as a Function Of Laser Energy Density.

Energy Density Joules/cm^2	Wafer #	1st Oxidation Lifetime, μsec		2nd Oxidation Lifetime, μsec	
		Gettered	None	Gettered	None
9.9	1	280.3		133.9	
	2	190.0	100.8	195.3	3.93
8.2	3	277.4	130.3	179.6	157.4
	4	606.7	3.2	55.4	3.5
6.5	5	35.0	8.6	31.6*	1.1
	6	11.7	40.7	37.6*	21.2
	7	94.5	211.7	138.3*	123.7
5.3	8	7.4	9.6	87.1*	21.5
	9	42.3	70.9	45.1*	1.8
	10	79.6	9.4	234.3*	2.9

*Laser damaged at 11.2 joules/cm^2 before second oxidation.

the lifetime degrades somewhat for the non-damaged halves, as summarized in Table I. However, lifetime improvement is obtained in the redamaged wafer halves. This result confirms that laser gettering is caused by the damage generated in the wafer. The minimum energy density required for achieving gettering is about 8 joules/cm^2. The corresponding damage depth for this energy is about 5 μm.

The effectiveness of laser gettering versus increased depth of damage was also investigated. In this experiment the damage depth was increased to approximately 20 μm. Such damage depth is obtained for an energy density of 33.3 joules/cm^2. Table II summarizes the results obtained for this power input using different line spacings. Using a line spacing of 0.5 and 1 mm the improvement in lifetime measured after the first oxidation is only minor and is negligible for line spacings of 2 and 5 mm. After the second oxidation, such deep laser damage causes lifetime degradation. The degradation increases as the scan line spacing decreases. It is obvious that too much laser damage (20 μm) causes lifetime degradation after high temperature processing. Such lifetime degradation is caused by dislocations which slip through the wafer thickness until they reach the wafer frontside. This is shown in Fig. 9 where dislocations generated by laser damage, for a line spacing of 1 mm, intersect a 1.5 mm MOS capacitor on the wafer frontside. As a result, lifetime degrades as shown in Table II.

TABLE II. The Effect of Damage Spacing and Multiple Oxidations on Laser Gettering

Damage Depth: 20 μm

Damage Spacing	Wafer #	1st Oxidation		2nd Oxidation	
		Lifetime, μsec		Lifetime, μsec	
		Gettered	None	Gettered	None
0.5mm	16	209	159	121	254
	17	233	151	123	169
	18	208	201	148	156
1 mm	19	745	571	397	328
	20	444	499	162	217
	21	424	334	219	283
2 mm	22	254	344	44	62
	23	415	342	135	100
	24	159	56	96	35
5 mm	25	253	237	239	212
	26	277	284	141	160
	27	265	163	219	107

The effect of multiple oxidations on the effectiveness of laser gettering, for a damage depth of 5 μm was also investigated and is shown in Table III. The damage is generated with an energy density of 9.9 joules/cm^2. Table III shows that in this case the average lifetime for the laser gettered halves is consistently a factor of two higher than the lifetime obtained for the non-gettered halves. No significant degradation in gettering effectiveness is observed after three oxidation cycles. According to such measurements, the optimum damage depth for gettering is 5 to 10 μm. To obtain such damage an energy density of 9 to 15 joules/cm^2 is required.

The effect of scan line spacing on laser gettering for a damage depth of 5 μm was also investigated and is summarized in Table IV. Table IV shows that the effectiveness of laser gettering tends to decrease as the damage spacing increases. This confirms that the effectiveness of laser gettering depends on the density of damage sites. According to our measurements, a practical line spacing is 0.5 to 1 mm.

4.0 DISCUSSION

The results of this study show that laser damage gettering arises from the defects and strain fields in the wafer produced by the incident beam. During subsequent high temperature processing, the strain is released through

TABLE III. The Effect of Mulitple Oxidations on Laser Gettering

Damage Depth: 5μm
Damage Spacing: 1mm

Wafer #	1st Oxidation		2nd Oxidation		3rd Oxidation	
	Lifetime, μsec Gettered	None	Lifetime, μsec Gettered	None	Lifetime, μsec Gettered	None
2	541.0	219.0	401.1	144.1	118.9	35.4
5	143.8	54.7	156.6	136.6	72.2	65.1
8	239.8	52.8	494.7	139.5	155.3	45.2
3	98.7	76.1	49.4	40.7		
6	104.3	63.8	167.5	83.6		
9	158.3	46.1	249.2	68.6		
4	566.8	238.8				
7	189.2	73.7				

TABLE IV. The Effect of Damage Spacing on Laser Gettering

Damage Depth: 5μm

Damage Spacing	Wafer #	Lifetime, μsec	
		Gettered	None
1 mm	1	697.1	483.7
	2	472.5	380.3
	3	407.8	323.7
2 mm	4	426.9	395.3
	5	56.6	0.064
	6	9.81	0.023
3 mm	7	166.5	83.6
	8	651.6	467.6
	9	270.0	120.8
4 mm	10	130.0	135.6
	11	92.5	54.3
	12	4.77	0.95

generation of dislocations. The dislocations act as effective gettering sites. The gettering mechanism is essentially the same as the one proposed for mechanical damage gettering (1,2), implantation damage gettering (3,4) and for surface layer deposition gettering (6). Important parameters which influence gettering most are damage depth and line spacing. The damage depth is precisely controlled through the incident laser power. For the laser power required to achieve only surface melting the damage depth is less than 1 μm. Under such conditions, the silicon recrystallizes through epitaxial regrowth during cooling and no crystal defects are generated during subsequent oxidation cycles. Consequently, laser gettering is small or not occurring. If the incident laser power is large enough misoriented grains, scratch-like damage, dislocations and stacking faults are generated in the wafer. During subsequent oxidations, these defects act as sources of dislocations. As a result, a high density of dislocations and dislocation loops is generated. These defects are effective gettering sites. Therefore, a significant improvement in lifetime is achieved. As the damage depth increases to 20 μm or more, the dislocations propagate during oxidation to the wafer frontside.

The effectiveness of laser gettering is also controlled by the scan line spacing. The line spacing determines the density of damage sites. As a result, the effectiveness of laser gettering increases with decreased line spacing.

5.0 CONCLUSIONS

The effectiveness of laser gettering depends on the amount of damage produced in the silicon. Important damage parameters are damage depth and line spacing. For low laser power, which leads only to surface melting, the amount of damage is small and gettering is not apparent. For larger laser power, which leads to silicon evaporation, damage is produced in the silicon and gettering becomes effective. The gettering arises from the strain fields and defects generated in the wafer surface through the local heating of the laser beam. During subsequent high temperature processings, the strain in the wafer is released through generation of additional dislocations. As a result, a significant improvement in lifetime is achieved. The effectiveness of laser gettering improves with an increased number of damage sites produced in the wafer. However, for too much damage (20 μm deep or more) a degradation in lifetime may occur. The degradation results from propagation of dislocations to the wafer frontside.

Optimum damage conditions for laser gettering are found for a damage depth of 5 to 10 μm and a line spacing of 0.5 to 1.0 mm. The correspondent energy density to produce this damage depth is 9 to 15 joules/cm^2.

6.0 REFERENCES

1. D. I. Pomerantz, J. Appl. Phys. 35, 695, (1964).

2. G. H. Schwuttke, K. H. Yang, and H. Kappert, Phys. Stat. Sol. (a) 42, 553, (1977).

3. B. Masters and J. Fairfield, Radiation Effects, 6, 57 (1970).

4. T. E. Seidel, R. L. Meek and A. G. Cullis, J. Appl. Phys. 46, 600 (1975).

5. W. R. Fahrner and C. P. Schneider, J. Electrochem, Soc. 123, 100 (1976).

6. P. M. Petroff, G. A. Rozgonyi, and T. T. Shang, J. Electrochem. Soc., 123, 565 (1976).

7.0 APPENDIX

HIGHLIGHTS

Chapter I

Minority carrier lifetime degradation in silicon, as a result of 200 keV argon and 80 keV silicon implantation, is measured after a 1h anneal in dry oxygen or a 30 minute anneal in nitrogen.

The lifetime degradation is studied for the implantation range of 10^{11} to 10^{16} ions/cm^2. For this range, a lifetime decrease spanning 5 orders of magnitude is observed. The decrease in lifetime is minor for a low implantation dose (10^{11} to 10^{12} ions/cm^2). It increases sharply with a higher dose. It levels off for the amorphization dose at a lifetime of approximately 10^{-10} seconds.

The lifetime degradation is different for argon and silicon implantations. For low argon implantations the decrease in lifetime is impurity controlled. At a higher dose the decrease in lifetime is caused by the argon impurity and by the crystal defects generated by the recrystallization of the amorphous layer.

For silicon implantations the decrease in lifetime is caused only by crystal defects. Lifetime degradation due to Si^+ implantation is only minor up to a dose of 10^{14} Si^+/cm^2.

After reaching the amorphization dose ($\sim 5 \times 10^{14}$ Si^+/cm^2) the lifetime drops rapidly to the 10^{-10} second level. Correspondingly, the number of crystal defects increases in the annealed implanted layer.

Lifetime recovery experiments, using gettering techniques (ISS), are not successful because they do not anneal out the defect state in the crystal caused by the high implantation (amorphization) dose.

Argon implantation of $\geq 10^{13}$ Ar^+/cm^2 leads to the formation of bubbles in the silicon lattice. It is shown that up to 92% of the implanted argon can be trapped in bubbles. Size and number of argon bubles increases with implantation dose. However, argon bubbles are shown to have only minor influence on lifetime degradation.

Low concentrations of oxygen, introduced through "knock-on" into the substrate, as a result of implantation through an oxide layer, are found to slow down the degradation of lifetime.

Chapter II

High energy argon and oxygen implantations on wafer backsides improve minority carrier lifetimes-measured by the MOS C-t technique-on wafer front sides.

High energy implantations produce buried damage layers under the silicon surface. Such buried damage layers are resistant to annealing cycles as encountered during standard semiconductor processing. Consequently, they provide more efficient gettering action as compared to damage layers produced by low energy implantations.

High energy argon gettering is found to be dependent on the implantation dose. Maximum gettering efficiency is obtained for high dose implantation ($>10^{14}$ Ar^+/cm^2) which leads to the formation of sub-surface amorphous layers.

Oxygen gettering shows no clear dose dependency. A remarkable gettering efficiency is already obtained for an implantation dose of 10^{11} $0^+/cm^2$.

TABLE OF CONTENTS